Charm Hadrons from Fragmentation and B decays in e^+e^- Annihilation at $\sqrt{s} =$10.6 GeV

R. Seuster,[6] K. Abe,[38] H. Aihara,[40] Y. Asano,[43] T. Aushev,[11] A. M. Bakich,[35]

M. Barbero,[6] I. Bedny,[1] U. Bitenc,[12] I. Bizjak,[12] A. Bozek,[24] M. Bračko,[7, 18, 12]

J. Brodzicka,[24] A. Chen,[21] B. G. Cheon,[3] Y. Choi,[34] A. Chuvikov,[32] S. Cole,[35]

J. Dalseno,[19] M. Danilov,[11] M. Dash,[44] L. Y. Dong,[9] J. Dragic,[7] A. Drutskoy,[4]

S. Eidelman,[1] F. Fang,[6] T. Gershon,[7] A. Go,[21] G. Gokhroo,[36] B. Golob,[17, 12]

A. Gorišek,[12] K. Hayasaka,[20] M. Hazumi,[7] Y. Hoshi,[38] S. Hou,[21] W.-S. Hou,[23]

T. Iijima,[20] K. Ikado,[20] R. Itoh,[7] Y. Iwasaki,[7] J. H. Kang,[45] J. S. Kang,[14] P. Kapusta,[24]

N. Katayama,[7] H. Kawai,[2] T. Kawasaki,[26] H. R. Khan,[41] H. Kichimi,[7] H. J. Kim,[15]

S. M. Kim,[34] P. Križan,[17, 12] P. Krokovny,[1] R. Kulasiri,[4] C. C. Kuo,[21] A. Kuzmin,[1]

Y.-J. Kwon,[45] J. S. Lange,[5] T. Lesiak,[24] J. Li,[33] S.-W. Lin,[23] F. Mandl,[10] W. Mitaroff,[10]

H. Miyake,[29] Y. Miyazaki,[20] R. Mizuk,[11] T. Nagamine,[39] Y. Nagasaka,[8] E. Nakano,[28]

M. Nakao,[7] S. Nishida,[7] O. Nitoh,[42] S. Ogawa,[37] T. Ohshima,[20] T. Okabe,[20]

S. Okuno,[13] S. L. Olsen,[6] Y. Onuki,[26] H. Ozaki,[7] P. Pakhlov,[11] H. Palka,[24]

C. W. Park,[34] H. Park,[15] K. S. Park,[34] R. Pestotnik,[12] L. E. Piilonen,[44] Y. Sakai,[7]

N. Sato,[20] T. Schietinger,[16] O. Schneider,[16] J. Schümann,[23] C. Schwanda,[10]

M. E. Sevior,[19] H. Shibuya,[37] V. Sidorov,[1] A. Somov,[4] N. Soni,[30] R. Stamen,[7]

S. Stanič,[27] M. Starič,[12] S. Y. Suzuki,[7] F. Takasaki,[7] K. Tamai,[7] N. Tamura,[26]

M. Tanaka,[7] G. N. Taylor,[19] Y. Teramoto,[28] X. C. Tian,[31] S. Uehara,[7] T. Uglov,[11]

K. Ueno,[23] S. Uno,[7] P. Urquijo,[19] G. Varner,[6] C. C. Wang,[23] C. H. Wang,[22]

M.-Z. Wang,[23] Q. L. Xie,[9] B. D. Yabsley,[44] A. Yamaguchi,[39] Y. Yamashita,[25]

M. Yamauchi,[7] J. Ying,[31] Y. Yusa,[39] L. M. Zhang,[33] Z. P. Zhang,[33] and V. Zhilich[1]

Typeset by REVTeX

1

(The Belle Collaboration)

[1] *Budker Institute of Nuclear Physics, Novosibirsk*

[2] *Chiba University, Chiba*

[3] *Chonnam National University, Kwangju*

[4] *University of Cincinnati, Cincinnati, Ohio 45221*

[5] *University of Frankfurt, Frankfurt*

[6] *University of Hawaii, Honolulu, Hawaii 96822*

[7] *High Energy Accelerator Research Organization (KEK), Tsukuba*

[8] *Hiroshima Institute of Technology, Hiroshima*

[9] *Institute of High Energy Physics,*
Chinese Academy of Sciences, Beijing

[10] *Institute of High Energy Physics, Vienna*

[11] *Institute for Theoretical and Experimental Physics, Moscow*

[12] *J. Stefan Institute, Ljubljana*

[13] *Kanagawa University, Yokohama*

[14] *Korea University, Seoul*

[15] *Kyungpook National University, Taegu*

[16] *Swiss Federal Institute of Technology of Lausanne, EPFL, Lausanne*

[17] *University of Ljubljana, Ljubljana*

[18] *University of Maribor, Maribor*

[19] *University of Melbourne, Victoria*

[20] *Nagoya University, Nagoya*

[21] *National Central University, Chung-li*

[22] *National United University, Miao Li*

[23] *Department of Physics, National Taiwan University, Taipei*

[24] *H. Niewodniczanski Institute of Nuclear Physics, Krakow*

[25] *Nippon Dental University, Niigata*

[26]*Niigata University, Niigata*

[27]*Nova Gorica Polytechnic, Nova Gorica*

[28]*Osaka City University, Osaka*

[29]*Osaka University, Osaka*

[30]*Panjab University, Chandigarh*

[31]*Peking University, Beijing*

[32]*Princeton University, Princeton, New Jersey 08544*

[33]*University of Science and Technology of China, Hefei*

[34]*Sungkyunkwan University, Suwon*

[35]*University of Sydney, Sydney NSW*

[36]*Tata Institute of Fundamental Research, Bombay*

[37]*Toho University, Funabashi*

[38]*Tohoku Gakuin University, Tagajo*

[39]*Tohoku University, Sendai*

[40]*Department of Physics, University of Tokyo, Tokyo*

[41]*Tokyo Institute of Technology, Tokyo*

[42]*Tokyo University of Agriculture and Technology, Tokyo*

[43]*University of Tsukuba, Tsukuba*

[44]*Virginia Polytechnic Institute and State University, Blacksburg, Virginia 24061*

[45]*Yonsei University, Seoul*

3

Abstract

We present an analysis of charm quark fragmentation at 10.6 GeV, based on a data sample of 103 fb^{-1} collected by the Belle detector at the KEKB accelerator. We consider fragmentation into the main charmed hadron ground states, namely D^0, D^+, D_s^+ and Λ_c^+, as well as the excited states D^{*0} and D^{*+}. The fragmentation functions are important to measure as they describe processes at a low energy scale, where calculations in perturbation theory lead to large uncertainties. Fragmentation functions can also be used as input distributions for Monte Carlo generators. Additionally, we determine the average number of these charmed hadrons produced per B decay at the $\Upsilon(4S)$ resonance and measure the distribution of their production angle in e^+e^- annihilation events and in B decays.

I. INTRODUCTION

Over recent years perturbative quantum chromodynamics (pQCD) has shown impressive agreement with various inclusive measurements at e^+e^- colliders at many center-of-mass energies (CME) ranging from 14 GeV up to 206 GeV. These measurements utilised variables called event shapes or jet rates, see [1] for such an analysis. These are inclusive variables, whose values are calculated from the four-momenta of all particles in an event.

Other properties, such as the momentum spectra of charged or neutral particles, have also been measured, but their prediction has proven to be more difficult. The necessary calculations have to cover the entire energy range from the production of the partons at the CME down to the scale of the hadron masses (typically 1 GeV/c^2), at which hadronisation occurs. Typically, powers of the form $\log(Q^2/m^2)$ arise when quark masses are taken into account, making pQCD calculations difficult to interpret.

Attempts have been made to extend the applicable range of pQCD to lower scales. These attempts have to be validated, for example by comparing so-called fragmentation functions. Due to the scaling violation of QCD, a fundamental property of this theory, the fragmentation function for a given particle depends explicitly on the CME. This energy dependence must follow the Dokshitzer-Gribov-Lipatov-Altarelli-Parisi (DGLAP) [2] evolution equations.

Thus, the fragmentation functions have to be properly evolved. Monte Carlo (MC) generators which include this scaling can be used instead of analytical evolution. Common MC generators which include this scaling are JETSET [3], (its variant) PYTHIA [4] and HERWIG [5].

These MC generators are also needed to model hadronisation, the transition of partons into hadrons, which cannot be calculated from first principles within QCD. Various models are implemented in MC generators. These can be distinguished by comparing the (identified) heavy hadron momentum spectra predicted by each model to the spectra seen

5

in data.

Fragmentation functions for heavy quarks are attractive both experimentally and theoretically. Concerning theory, mass effects in the matrix elements only have to be considered for the heavy quark; in the limit of $m_{light} \to 0$, a pQCD calculation based on an effective Lagrangian reduces the complexity of the calculation compared to the case of light quark fragmentation.

Experimentally, it is important to measure heavy quark fragmentation functions as their shapes are different from the corresponding functions for light quarks; such a measurement is furthermore straightforward, as very often hadrons containing heavy quarks can easily be identified. Since the production of heavy quarks is strongly suppressed in both the perturbative splitting of one parton to many partons (the so-called "parton shower") and in hadronisation, a heavy quark found in an event will most likely be produced in the primary interaction.

At LEP and SLD, b quark fragmentation functions have been measured with high precision [6, 7, 8, 9]. These measurements found that these fragmentation functions are in fact close to the ones of light quarks, suggesting that one combined model for all five flavours might describe the measured momentum spectra better than functions which have been introduced for heavy quarks alone. These collaborations have also published measurements of c quark fragmentation functions [10, 11], but with large statistical uncertainties due to the small product of the branching fraction and reconstruction efficiency for the various final states. Some commonly used fragmentation functions are described by the models of Peterson *et al.* [12], of Kartvelishvili *et al.* [13] and of Collins and Spiller [14], as well as by the models of the Lund group [15] and one of its variants by Bowler [16].

For charm quark fragmentation functions at lower energies, the most recent published results for D^0, D^+, D^{*0} and D^{*+} are those of CLEO [17]. The analysis presented here has better statistical precision as the data sample is five times larger. Other measurements are more than 10 years old [18, 19]; their data sample is over three orders of magnitude

smaller than that used in this analysis. The systematic uncertainties are reduced significantly and are comparable to those in [17]. For a recent review of fragmentation function measurements and theory, see [20].

A measurement of D^0 and D^+ performed by the same experiment on the same data set allows for an easy comparison of charged meson production rates and momentum spectra, as well as a comparison of the momentum-dependent production of secondary-to primary-produced mesons. The measurement of the excited states D^{*0} and D^{*+} allows the determination of the feed-down contribution to the ground states D^0 and D^+ and also a momentum-dependent determination of $V/(V + P)$, the ratio of the production rates of vector and the sum of vector and pseudo-scalar mesons. A comparison between D_s^+ production, and the production of D^0 and D^+, can be used to determine the fraction of s quark production in hadronisation. Comparing the results for the Λ_c^+ to those of the D mesons makes a study of the baryon production mechanism possible.

In addition to charm fragmentation in the $e^+e^-\to c\bar{c}$ continuum, charmed hadrons in e^+e^- annihilation events can be produced in decays of b-hadrons. The dataset for this analysis includes events above the production threshold for $B\bar{B}$ pairs, at the $\Upsilon(4S)$ resonance, so the lower momentum hadrons include contributions from B^0 and B^+ decays. This allows a measurement of the production rate of charmed hadrons in B-meson decay.

II.   DATA SAMPLE AND EVENT SELECTION

This analysis uses data recorded at the Belle detector at the KEKB accelerator. The KEKB e^+e^- collider is a pair of storage rings for electrons and positrons with asymmetric energies, $8.0\,\mathrm{GeV}$ (e^-) and $3.5\,\mathrm{GeV}$ (e^+), and a single intersection point with a 22 mrad crossing angle. The beam energies are tuned to produce an available CME of $\sqrt{s} = 10.58$ GeV, corresponding to the mass of the $\Upsilon(4S)$. A detailed description can be found in [21].

The Belle detector covers a solid angle of almost 4π. Closest to the interaction point is a high resolution silicon micro-vertex detector (SVD). It is surrounded by the central drift chamber (CDC). Two dedicated particle identification systems, the aerogel Čerenkov counter (ACC) and the time-of-flight system (TOF), are mounted between the CDC and the CsI(Tl) crystal electromagnetic calorimeter (ECL). All these sub-detectors are located inside a super-conducting coil that provides a magnetic field of 1.5 T. The return yoke of the coil is instrumented as a K_L^0 and μ detector. A detailed description can be found in [22].

This analysis uses 87.7 fb^{-1} of e^+e^- annihilation data taken at the $\Upsilon(4S)$ resonance at $\sqrt{s} = 10.58$ GeV ("on-resonance data"), above the production threshold for $B\bar{B}$ pairs. Additional 15.0 fb^{-1} are taken 60 MeV below the resonance at $\sqrt{s} = 10.52$ GeV ("continuum data"), which is also below the production threshold for $B\bar{B}$ pairs. Hadronic events are selected as described in [23]. The selection efficiency of events originating from light quarks (d, u and s) passing this hadronic preselection has been estimated to be 84.0%, using 9.6×10^6 MC events. For c quarks, the efficiency has been determined with 6.6×10^6 MC events to be 93.0%. The light quark sample contains almost no true candidates, reflecting the small rate for gluon splitting into open charm states, i.e. two mesons containing c quarks.

To estimate the efficiency of reconstructing charmed hadrons and to correct for distortions due to the finite acceptance of the detector, MC samples of $e^+e^- \rightarrow c\bar{c}$ events corresponding to a data luminosity of 217 fb^{-1} (approximately 2 1/2 times the on-resonance data), and $e^+e^- \rightarrow q\bar{q}$ ($q = u$, d and s) events corresponding to 18 fb^{-1} (approximately 1.2 times the continuum data), have been studied. The MC samples were generated using the QQ98 generator [24] employing the Peterson fragmentation function for c quarks and were processed through a detailed detector simulation based on GEANT 3.21 [25]. This sample will be referred to as the generic sample. Special samples of several million $e^+e^- \rightarrow c\bar{c}$ events were generated with the EvtGen [26] generator using the Peterson as

8

well as the Bowler fragmentation functions and were also run through the detector simulation. These samples will be referred to as reweighted samples; see Section VI C for details about the reweighting procedure. For each charmed hadron used in this analysis, a sample was generated where that hadron was forced to decay in the same channel as later reconstructed. These samples were reconstructed using the same procedures as for data.

A. Particle Identification

To minimise possible kinematic biases due to tight selection criteria for identified particles, only loose cuts on the particle identification of the stable particles have been applied. All particles with mean lifetime longer than 100 ps have been called "stable". Apart from reducing a potential kinematic bias, this increased the reconstruction efficiency at the cost of introducing more background, especially in the low momentum region.

In general, the identification for each track was based on one or more likelihood ratios, which combined the information from the time-of-flight and Čerenkov counters and the energy loss dE/dx in the drift chamber. Pions and kaons were separated by a single likelihood ratio $\mathcal{L}(K)/(\mathcal{L}(K) + \mathcal{L}(\pi))$. Charged particles were identified as pions if this ratio was less than 0.95 and as kaons if this ratio was larger than 0.05. This overlap allowed a charged particle to be identified as both a pion and a kaon, potentially resulting in identifying a mother (candidate) particle as its own anti-particle (*i.e.*, a $D^0 \to K^-\pi^+$ decay could be identified as a $\overline{D}^0 \to \pi^-K^+$ decay), and therefore overestimating the number of candidates. As this misidentification was only possible for neutral particles, an additional systematic uncertainty has been assigned for the D^0 and D^{*0}; see section IV for details.

For proton identification, similar likelihood ratios were required to fulfil $\mathcal{L}(p)/(\mathcal{L}(p) + \mathcal{L}(\pi)) > 0.6$ and $\mathcal{L}(p)/(\mathcal{L}(p) + \mathcal{L}(K)) > 0.6$. For the π^0, photon candidates

with energies above 30 MeV were combined to form a π^0 candidate. Under the assumption that the π^0 candidate decayed at the interaction point, it was required to have an invariant mass consistent with the π^0 mass.

The efficiencies ϵ and misidentification probabilities f for tracks from signal candidates under these cuts have been measured in data, and are listed in Table I; in all cases except the proton, $\epsilon > 95\%$ and $f \leq 26\%$. For kaons and pions the efficiencies and misidentification probabilities have been estimated in bins of the particle's momentum from D^{*+} and subsequent $D^0 \rightarrow K^- \pi^+$ decays; for protons, Λ decays have been used. The observed momentum spectra in data have been used to derive the listed numbers.

TABLE I: Typical efficiencies and misidentification probabilities for tracks from signal candidates used in this analysis. The misidentification probabilities listed under $\pi^\pm$ means the probability of mis-identifying it as a $K^\pm$.

	$\pi^\pm$	$K^\pm$	p
D^0 ($\epsilon|f$)	(96%|26%)	(96%|26%)	–
D^+ ($\epsilon|f$)	(96%|12%)	(97%|24%)	–
D_s^+ ($\epsilon|f$)	(98%|17%)	(97%|21%)	–
Λ_c^+ ($\epsilon|f$)	(98%|15%)	(97%|21%)	(81%|7%)

In addition to the requirements on the particle identification, all tracks had to be consistent with coming from the interaction point (IP). For the slow pion from the $D^{*+} \rightarrow D^0 \pi^+$ decay, all track quality and particle identification requirements were removed to increase the efficiency.

B. Reconstruction of charmed Hadrons

The reconstructed hadron decay chains used in this analysis are the following:

$D^0 \rightarrow K^-\pi^+$, $D^+ \rightarrow K^-\pi^+\pi^+$, $D_s^+ \rightarrow \phi\pi^+$ ($\phi \rightarrow K^+K^-$), $\Lambda_c^+ \rightarrow p^+K^-\pi^+$,

$D^{*+} \rightarrow D^0\pi^+$ ($D^0 \rightarrow K^-\pi^+$), $D^{*+} \rightarrow D^+\pi^0$ ($D^+ \rightarrow K^-\pi^+\pi^+$) and

$D^{*0} \rightarrow D^0\pi^0$ ($D^0 \rightarrow K^-\pi^+$).

The inclusion of charge-conjugate modes is implied throughout this paper and natural units are used throughout. For all charmed ground state hadrons, candidates whose masses were within 50 MeV/c^2 of their respective nominal mass were considered. For the intermediate D^0 and D^+ coming from the excited states D^{*0} and D^{*+} a mass window of 15 MeV/c^2 around the nominal masses of the D^0 and the $D^+$was chosen. Additionally, the selection window for the two excited states was tightened to 15 MeV/c^2 around the nominal mass difference between the excited meson and the D^0 or D^+. For the intermediate ϕ from the D_s^+ decay, the mass window was chosen to be 7 MeV/c^2. Multiple candidates for each particle and anti-particle were removed by a best candidate selection. Most false D^{*0} and D^{*+} candidates were formed from a true D^0 and a random slow pion. Therefore, the slow pions were used to determine the best candidate. For the neutral slow pion, the smallest χ^2 of the vertex fit was used. For the charged slow pion, the smallest distance to the IP of all hits used in the reconstruction was used. For all other charmed mesons, the selection was based on the particle identification of the kaon. In the rare case that multiple candidates were formed with the same kaon, the first candidate was randomly chosen.

III. ANALYSIS PROCEDURE

There are two variables commonly used in the measurements of fragmentation functions. These are the scaled energy $x_E = E_{candidate}/E_{candidate}^{MAX}$ and the scaled momentum $x_P = |\vec{p}_{candidate}|/|\vec{p}_{candidate}^{MAX}|$, where $E_{candidate}^{MAX} = \sqrt{s}/2$, $|\vec{p}_{candidate}^{MAX}| = \sqrt{s/4 - m_H^2}$, and m_H de-

TABLE II: The values for the masses or mass differences and branching fractions for all charmed hadrons used in this analysis. The masses are used only to shift the mass or the mass difference distributions in order to center their peaks near zero, therefore no errors are assigned. The branching fractions are taken from [28].

hadron	decay mode	mass [GeV/c^2]	product branching fraction
D^0	$K^-\pi^+$	1.8645	0.0380 ± 0.0009
D^+	$K^-\pi^+\pi^+$	1.8693	0.092 ± 0.006
D_s^+	$\phi\pi^+$	1.9685	$(0.036 \pm 0.009) \cdot (0.491 \pm 0.006)$
Λ_c^+	$p^+K^-\pi^+$	2.2849	0.050 ± 0.013
D^{*+}	$D^0\pi^+$	0.1455	$(0.677 \pm 0.005) \cdot (0.0380 \pm 0.0009)$
	$D^+\pi^0$	0.1407	$(0.307 \pm 0.005) \cdot (0.092 \pm 0.009)$
D^{*0}	$D^0\pi^0$	0.1422	$(0.619 \pm 0.029) \cdot (0.0380 \pm 0.0009)$

notes the mass of the charmed hadron. For b quarks at higher CMEs, the scaled energy x_E is often used. In this case, the mass of the B hadron reduces only slightly the allowed range at small x_E. For charmed hadrons at 10.58 GeV the range of x_E is significantly reduced; hence x_P is prefered and will be used in this analysis. Unless otherwise stated, all variables are given in the e^+e^- rest frame, taking into account the different beam energies for the on-resonance and the continuum samples.

For various bins in the range from 0.0 to 1.1 in the scaled momentum x_P, the signal yield has been determined from a fit to the mass or mass difference distributions of all candidates within the aforementioned selection windows. The finite momentum resolution of the detector can result in events being recorded in the region above the naïve limit of $x_P=1$, however, in the case of D^*, the principal contribution is due to the process $e^+e^- \rightarrow D^*D$. See Section V C for details.

A bin width of 0.02 in x_P has been chosen for all particles as a compromise between the statistical precision in each bin and the momentum resolution, which is a factor of two smaller. Additionally, to investigate the high x_P region around and above the naïve limit of $x_P=1$, the bin width has been decreased to 0.01; an expanded view of the region $0.90 < x_P < 1.05$ with this binning will be discussed in Section V C. Since this decreased bin width is still larger than, but comparable to, the momentum resolution, an unfolding using the singular-value-decomposition (SVD) approach [27] was tried in addition to the normal bin-by-bin correction and is discussed in Section V C.

The mass or mass difference distributions were parametrized by a single Gaussian, except for the $D^{*+} \rightarrow D^0 \pi^+$ decay channel where a double Gaussian was employed. For the mass distributions, the background was parametrized by a quadratic function; for $x_P > 0.9$ a linear function was found to be sufficient to fit the considerably lower background. For the mass difference distributions of the excited D mesons, a phase-space-like function $f(\Delta m) = a(\Delta m - \Delta M_0)^b$ was used with a and b being free parameters and ΔM_0 the nominal difference between the mass of the excited mother particle and that of the ground state charm meson.

For all charmed hadrons, the mean mass m_i and the width μ_i of the signal Gaussian was fitted separately for MC, continuum and on-resonance data. For these fits, x_P was divided into 4 bins from $0.2 < x_P < 1.0$ with a constant bin size of 0.2. In a second fit, two quadratic functions $m_i(x_P)$ and $\mu_i(x_P)$ were fitted to the results of the first fit in these four bins. For the distributions with a bin width of 0.02 and 0.01 in x_P, the mean and width parameters in the fit were fixed to the values of the quadratic functions $m_i(x_P)$ and $\mu_i(x_P)$ for the appropriate x_P value.

For the $D^{*+} \rightarrow D^0 \pi^+$ decay mode full correlations between the two Gaussians of the signal function were taken into account when determining the fit yield.

When combining the on-resonance data with the continuum data, two corrections have been applied to the on-resonance data. After normalising using the integrated luminosities

13

of the respective samples, the naïve $1/s$ dependence on the total hadronic cross section has been taken out by multiplying the distributions of the on-resonance sample by the square of the ratio of the CME's, namely by $(10.58 \text{ GeV}/10.52 \text{ GeV})^2$. Second, from MC an additional correction of $+0.27\%$ due to different initial state radiation (ISR) at the two energy points has been applied to the on-resonance samples. This correction was based on a MC study of the total cross sections at these two energy points.

A. x_P-dependent Mass Fits

Fig. 1 and Fig. 2 show the mass distributions of all charmed hadrons reconstructed in this analysis for two representative bins in x_P. The x_P bins shown are $0.28 < x_P < 0.30$ in Fig. 1 and $0.68 < x_P < 0.70$ in Fig. 2. They represent a low x_P bin with higher background and a bin close to the maximum of the x_P distribution with less background, respectively. All mass (mass difference) distributions have been shifted by their nominal mass (mass difference) to center the peaks at zero. See table II for the masses used. Note that the scale on the y-axis does not start at zero in the upper four plots in Fig. 1 and Fig. 2.

For $0.28 < x_P < 0.30$ (shown in Fig. 1), the mass distributions for the D^0 and D^+ ground states and the mass difference distributions for the excited states show clear peaks at the expected value for signal. Compared to higher x_P values, the background is higher due to a larger amount of combinatorial background, and the signal-to-background ratio is lower. At higher x_P values, such as those shown in Fig. 2 ($0.68 < x_P < 0.70$), the background is considerably reduced, whereas the signal yield is enhanced. This significantly increased the signal-to-background ratio.

14

B.   Raw Signal Yield

Fig. 3 shows the signal yields as a function of x_P for all charmed hadrons, not corrected for the reconstruction efficiencies and for the branching fractions, denoted with "B" in the plots. For all particles, the contribution from B decays is clearly visible in the low x_P range, which is $x_P < 0.5$ for all charmed mesons containing a light quark as the spectator. For D_s^+ from B decays, the upper bound is approximately $x_P \sim 0.4$, reflecting the energy required to produce an additional strange quark. Contributions from the $b \rightarrow u$ transition, where the D_s^+ is formed at the upper vertex, can populate the region up to $x_P = 0.5$, but are strongly suppressed. For the Λ_c^+, the only baryon reconstructed in this analysis, the upper bound is further decreased to approximately $x_P \sim 0.37$, due to the production of an additional anti-baryon.

All distributions peak around $x_P \sim 0.6 - 0.7$ and show similar shapes.

C.   Efficiency Correction

The efficiencies were determined from MC and are defined as the appropriate raw signal yield (determined by the same procedure as for data) divided by the generated MC x_P distribution. The seven histograms in Fig. 4 show the x_P-dependent efficiency of each charmed hadron used in this analysis for continuum data and on-resonance data. The D^0 efficiency is close to 50% and almost constant over the entire x_P range. The efficiency for $D^{*+} \rightarrow D^0 \pi^+$ approaches the D^0 efficiency at high values of x_P and diminishes at lower values of x_P, reflecting the reduced efficiency of reconstructing low-momentum pions. The two D^* decay modes that include a neutral slow pion show a different behaviour: the efficiencies stay constant over a wide range of about $0.3 < x_P < 1$ and below $0.3 < x_P$ the efficiency increases for $x_P \rightarrow 0$ due to the increasing reconstruction efficiency for slow π^0.

15

The reconstruction efficiencies for the three-particle decay modes do not show a strong dependence on x_P, slightly varying between 15% and 20% for the D_s^+ and remaining constant at about 30% for the Λ_c^+. The decreasing efficiency for particles at values close to the kinematic limit is an artefact of the decreasing statistics in all generic MC samples. The reweighted samples, which were generated with a different fragmentation function than the generic samples, contain significantly more events in the very high x_P region and do not show such behaviour. This difference between the two efficiency estimates was added to the systematic uncertainty.

The efficiency is a function of the production angle, which differs for charmed hadrons from B decays and from continuum events. For the on-resonance samples, the efficiency has been determined by a luminosity-weighted mixture of charmed MC and dedicated samples containing decays of charged and neutral B mesons. For the continuum sample, only charmed MC was used.

In data, it was verified that D^{*+} produced in e^+e^- annihilation are unpolarised by verifying that the distribution of the cosine of the helicity angle is flat. The helicity angle is defined as the angle between the slow charged pion in the D^{*+} rest frame and the flight direction of the D^{*+} in the center of mass system of the event. Because the efficiency for $D^{*+} \rightarrow D^0 \pi^+$ strongly depends on the momentum distribution of the slow π^+, which in turn depends on the helicity angle, polarised D^{*+} can introduce a bias into the efficiency correction.

IV. SYSTEMATIC UNCERTAINTIES

Various sources of systematic uncertainties have been considered:

Uncertainties due to tracking were estimated to be 1% per track using a sample of partially reconstructed D^{*+} decays. As the uncertainty increased at very low momentum,

16

the estimated momentum-dependent uncertainty of the slow charged pion was folded with the observed momentum spectrum. The systematic uncertainty due to the slow neutral pion detection efficiency was assessed by examining the differences in the shapes of the fragmentation function of the two D^{*+} decay modes, $D^{*+} \to D^0 \pi^+$ and $D^{*+} \to D^+ \pi^0$.

Uncertainties due to the modeling of ISR in the MC were determined by restricting the longitudinal momentum in the laboratory frame of all candidates to $p_z^{lab} > 0$ only. This cut preferentially removed events with ISR photons in the negative z direction, potentially introducing an artificial asymmetry. The z direction is defined as being anti-parallel to the positron beam, which coincides up to corrections due to the crossing angle with the boost vector into the e^+e^- rest-frame.

The cut on the likelihood ratios for kaon and proton candidates was tightened to 0.2 and 0.8, respectively, and the difference was taken into account in the systematic uncertainty.

Potential differences between the actual signal shape and the fitting function were estimated by determining the signal yield with a counting method instead of using the fit. Here, the number of entries in the mass (mass difference) distribution was counted in a window about one third the size of the total 50 MeV/c^2 (15 MeV/c^2) window around the peak position, corresponding to roughly three times the resolution. The number of background events was subtracted after integrating the background function of the standard fit within the same mass window.

An additional flavour assignment systematic uncertainty was taken into account for the neutral states D^0 and D^{*0}. The loose cuts on the charged pion and kaon particle identification allowed a D^0 to be identified as a $\overline{D}^0$: the flavour of the D^0 from D^{*+} decays was identified by the charge of the slow pion (except for a small contribution from doubly-Cabibbo-suppressed decays). In the MC sample, the likelihood ratio of the pion candidate was larger than that of the kaon candidate for 1.3% of all D^0 candidates; the corresponding fraction was determined to be 1.1% for D^{*+} decays. The statistical uncertainties on these numbers are less than 0.05%. Accordingly, a difference of 0.2% was

assigned as the uncertainty of the flavour assignment due to the overlap of the pion and kaon likelihoods of the particle identification.

The luminosity of the data sample was determined to have an uncertainty of about 1.4%. A corresponding scale uncertainty of 1.4% was assigned to the normalisation of the shape. It has been checked that the normalisation of the fragmentation functions of the on-resonance and continuum sample agree with each other, and their difference of 0.94% is well within the scale uncertainty.

Finally, the reconstruction efficiencies of the generic and the reweighted samples differed slightly. This small difference was added to the systematic uncertainty.

All systematic uncertainties were added in quadrature to give the total systematic uncertainty.

V. RESULTS

In this section, various results for the charmed hadrons are presented.

A. x_P Distributions

Fig. 5 shows the efficiency-corrected x_P distributions for the different particles for e^+e^- annihilation events, *i.e.* spectra of hadrons formed in the fragmentation of charm quarks. Above $x_P > 0.5$, the differential x_P distributions of the on-resonance sample and the continuum sample have been combined by a weighted average, where the inverse of the squared statistical uncertainty was used as the weight. As the systematic uncertainties for both samples are highly correlated, the larger uncertainty of the on-resonance and the continuum samples was used for the combined sample.

As most efficiencies do not depend strongly upon x_P, the shapes of the efficiency-corrected distributions are similar to those of the uncorrected distributions. All distributions peak around $x_P \sim 0.6 - 0.7$. To determine the peak position, a direct fit of the

18

data to the Peterson fragmentation function was tried. The shape of the data agreed very poorly as this model does not include gluon radiation or decays from higher resonances. Therefore, a Gaussian function was used to determine the peak position. The fit ranges were chosen from $x_P = 0.4$–0.8. The results of the fits are listed in Table III, together with the statistical and systematic uncertainties. The statistical uncertainty was determined by the RMS of the distribution divided by $\sqrt{N}$.

TABLE III: The peak positions of all hadrons, fitted with a Gaussian near the peak position. The fit range was $0.4 < x_P < 0.8$. Above $x_P > 0.5$, the continuum sample and the on-resonance sample have been combined. The given errors are the statistical and systematic uncertainties, respectively.

	$x_P{}^{\text{PEAK}}$
$D^0 \to K^- \pi^+$	$0.587 \pm 0.001 \pm 0.002$
$D^+ \to K^- \pi^+ \pi^+$	$0.600 \pm 0.001 \pm 0.001$
$D_s^+ \to \phi \pi^+$	$0.681 \pm 0.002 \pm 0.003$
$\Lambda_c^+ \to p^+ K^- \pi^+$	$0.612 \pm 0.001 \pm 0.004$
$D^{*+} \to D^0 \pi^+$	$0.631 \pm 0.001 \pm 0.002$
$\to D^+ \pi^0$	$0.618 \pm 0.011 \pm 0.023$
$D^{*0} \to D^0 \pi^0$	$0.631 \pm 0.001 \pm 0.003$

B. Average Number of Charmed Hadrons per B Decay

The x_P distributions of the on-resonance and continuum samples differ in the contribution from B decays for $x_P < 0.5$. Fig. 6 shows this difference: the differential x_P

19

distribution of the continuum sample was subtracted from that of the on-resonance sample. Thus, up to statistical fluctuations it contains only contributions from decays of B mesons.

Table IV lists the average number of charmed hadrons per B meson decay together with the present world average [28]. In order to determine the average number of charmed hadrons produced per B decay, we take the difference between the production rate in the on-resonance and the continuum sample and normalise by the B meson production cross section, which is estimated to be (1.073 ± 0.019) nb based on the measured luminosity and the measured number of $B\overline{B}$ pairs in this sample. Note that this visible production cross-section depends strongly upon the energy spread of the accelerator. The uncertainties in Table IV are from the limited statistics (first), the systematics as discussed in Section IV (second), and the luminosity measurement and the uncertainties on the branching fractions (third). Note that the luminosity measurement and the determination of the number of $B\bar{B}$ are strongly correlated. Both values agree well within one standard deviation with each other, only the average number of produced D^{*0}'s here is lower by about one standard deviation and is closer to that of D^{*+}'s.

The small bump seen in the x_P distributions of the charmed mesons except the D_s^+ at $x_P = 0.35$ is due to two body decays of the B mesons such as $B \to D^0 D^{(*)}$ in case of the D^0.

C. High x_P Region

An expanded view of the high x_P region is shown in Fig. 7. The downward triangles show the efficiency-corrected data; the upward triangles show the corrected and unfolded data.

Unfolding was done using the singular-value-decomposition (SVD) method [27]. From

TABLE IV: The average number $N_{B \to c}$ of charmed hadrons per B meson decay, corrected for acceptance and reconstruction efficiencies. The listed uncertainties are statistical, systematic, and the one due to the uncertainties on the branching fractions of the decays involved as well as on the luminosity, respectively.

	$N_{B \to c}$	PDG(2004)
$D^0 \to K^- \pi^+$	$0.644 \pm 0.003 \pm 0.024 \pm 0.021$	0.640 ± 0.030
$D^+ \to K^- \pi^+ \pi^+$	$0.248 \pm 0.004 \pm 0.033 \pm 0.020$	0.235 ± 0.019
$D_s^+ \to \phi \pi^+$	$0.122 \pm 0.015 \pm 0.033 \pm 0.030$	0.105 ± 0.026
$\Lambda_c^+ \to p^+ K^- \pi^+$	$0.042 \pm 0.011 \pm 0.033 \pm 0.018$	0.064 ± 0.011
$D^{*0} \to D^0 \pi^0$	$0.217 \pm 0.014 \pm 0.020 \pm 0.018$	0.260 ± 0.027
$D^{*+} \to D^0 \pi^+$	$0.218 \pm 0.007 \pm 0.020 \pm 0.015$	0.225 ± 0.025
$\to D^+ \pi^0$	$0.202 \pm 0.014 \pm 0.022 \pm 0.018$	0.225 ± 0.025
$average\ D^{*+}$	$0.215 \pm 0.006 \pm 0.022 \pm 0.016$	0.225 ± 0.025

MC, we determined the response matrix of the detector for producing for a certain true input value of $x_{P,true}$ a measured value of $x_{P,measured}$. This matrix was decomposed using the SVD into two orthogonal and one diagonal matrices which can easily be inverted. Inverting the diagonal matrix was limited by a criteria defined in [27] to contain only elements, which are of statistical significance.

The hatched histogram show the only process $e^+ e^- \to D^{*+} D^-$, the open histogram shows the sum of the previous process and $e^+ e^- \to D^{*+} D^{(*)-}$.

The x_P distributions for the ground states D^0, D^+, D_s^+ and Λ_c^+ extend up to the naïve kinematic endpoint $x_P = 1$ and no significant number of events are present for $x_P > 1$.

All three x_P distributions for the excited D mesons, however, show an enhancement at $x_P > 1$. These events above $x_P = 1$ correspond to events of the processes

$e^+e^- \to D^{*+}D^{(*)-}$ or $e^+e^- \to D^{*0}D^{(*)0}$ and are in good agreement with the measured cross sections [29] of $0.55 \pm 0.03 \pm 0.05$ pb for $e^+e^- \to D^{*+}D^-$ and $0.62 \pm 0.03 \pm 0.06$ pb for $e^+e^- \to D^{*+}D^{*-}$. Note that these events populate $x_P > 1$ only because of the use of the simplified upper limit $|\vec{p}_{candidate}^{MAX}|$, for producing two D^* mesons. A background fluctuation producing an artificial peak is unlikely for two reasons. First, at high x_P, the background is negligible, and second, the unfolding procedure tends to identify signals at the edge of a distribution as statistical fluctuations rather than real signals, thus decreasing the significance of the signals.

D. Total Production Cross-Section

The total production cross-section is given by the integral of the x_P distribution. This integral was determined for the continuum sample using the current value of the world average product branching fraction of each particle, see Table II and [28]. The results are listed in Table V, where the third error component reflects the uncertainty on the product branching fraction.

The results by CLEO [17] given in the last column used their own branching fractions, which differ slightly from the world averages used here. The results, however, agree well with each other. Another measurement by BaBar [30] is given in the same column. The total production cross-section for the D^{*0} differs only slightly from that of the D^{*+}. This can be understood as resulting from different feed-down contributions from higher resonances.

22

TABLE V: The total production cross-sections $e^+e^- \to DX$ (or Λ_c^+X), which have been corrected using the current world average of the respective product branching fractions. The listed uncertainties are statistical, systematic and the uncertainty due to the uncertainty on the branching ratios. Other measurements of production cross-sections are listed. The third column shows measurements by CLEO [17], BaBar [30] (marked [1]) and an older CLEO measurement [18] (marked [2]).

X	σ_{PROD} [pb]	$\sigma_{PROD(CLEO'04/BaBar)}$ [pb]
$D^0 \to K^-\pi^+$	$1449 \pm 2 \pm 64 \pm 38$	$1521 \pm 16 \pm 62 \pm 36$
$D^+ \to K^-\pi^+\pi^+$	$654 \pm 1 \pm 36 \pm 46$	$640 \pm 14 \pm 35 \pm 43$
$D_s^+ \to \phi\pi^+$	$231 \pm 2 \pm 92 \pm 77$	$210 \pm 6 \pm 9 \pm 52$[1]
$\Lambda_c^+ \to p^+K^-\pi^+$	$189 \pm 1 \pm 66 \pm 66$	$270 \pm 90 \pm 70$[2]
$D^{*0} \to D^0\pi^0$	$510 \pm 3 \pm 84 \pm 39$	$559 \pm 24 \pm 35 \pm 39$
$D^{*+} \to D^0\pi^+$	$598 \pm 2 \pm 77 \pm 20$	$583 \pm 8 \pm 33 \pm 14$
$D^{*+} \to D^+\pi^0$	$590 \pm 5 \pm 78 \pm 53$	-
average D^{*+}	$597 \pm 2 \pm 78 \pm 25$	-

E. Mean Values for x_P and Moments

In addition to the peak position for the seven x_P distributions, the mean and higher moments of these distributions were determined from distributions in $(x_P)^n$ with a bin width of 0.02 in x_P and a bin-by-bin efficiency correction was applied. The nth moment was determined by the mean of the efficiency corrected distributions in $(x_P)^n$, and its statistical uncertainty was determined by $\sigma/\sqrt{N_0}$, where N_0 is the number of entries in the uncorrected $(x_P)^n$ distribution. Tables VI and VII show the moments for the different decay modes.

TABLE VI: The first three moments of the x_P distribution for the seven particles/decay modes used in this analysis. The listed uncertainties are statistical and systematic uncertainties.

	$\langle x_P \rangle \times 1000$	$\langle x_P{}^2 \rangle \times 1000$	$\langle x_P{}^3 \rangle \times 1000$
$D^0 \to K^- \pi^+$	$570.33 \pm 0.18 \pm 2.23$	$353.98 \pm 0.29 \pm 2.50$	$233.85 \pm 0.28 \pm 2.54$
$D^+ \to K^- \pi^+ \pi^+$	$578.03 \pm 0.18 \pm 1.47$	$363.42 \pm 0.29 \pm 1.58$	$243.58 \pm 0.27 \pm 1.58$
$D_s^+ \to \phi \pi^+$	$635.34 \pm 0.47 \pm 4.22$	$442.52 \pm 0.81 \pm 8.64$	$323.52 \pm 0.83 \pm 11.14$
$\Lambda_c^+ \to p^+ K^- \pi^+$	$582.45 \pm 0.39 \pm 2.53$	$364.94 \pm 0.63 \pm 3.40$	$239.59 \pm 0.59 \pm 2.24$
$D^{*+} \to D^0 \pi^+$	$612.17 \pm 0.36 \pm 1.43$	$407.96 \pm 0.61 \pm 2.01$	$286.97 \pm 0.60 \pm 3.38$
$\to D^+ \pi^0$	$586.06 \pm 0.37 \pm 16.10$	$380.99 \pm 0.64 \pm 17.89$	$266.49 \pm 0.62 \pm 17.05$
$D^{*0} \to D^0 \pi^0$	$607.63 \pm 0.42 \pm 6.07$	$401.98 \pm 0.69 \pm 5.60$	$282.65 \pm 0.68 \pm 5.90$

F. Production Angle

Taking the interference between the exchange of virtual photons and Z bosons into account, the differential cross section for $e^+ e^- \to c\bar{c}$ is modified from the $1 + \cos^2 \theta$ form of the Born amplitude for pure photon exchange:

$$\frac{d\sigma}{d\cos\theta} = \frac{3}{8}(1 + \cos^2 \theta)\sigma_T + \frac{3}{4}\sin^2 \theta \sigma_L + \frac{3}{4}\cos \theta \sigma_A \tag{1}$$

Here, θ describes the angle between the incoming electron beam and the outgoing hadron containing the charmed quark, as measured in the CM frame. The term σ_T describes the contribution of pair production of spin-1/2 particles from transverse polarised vector bosons, the term σ_L the contribution from longitudinal polarised vector bosons and the term σ_A denotes the parity violating asymmetry due to the interference between Z bosons and virtual photons.

The $\mathcal{KK}$ MC generator [31] was used to predict the production angle distributions for the different charmed hadrons. This MC generator includes interference between initial

TABLE VII: The fourth through the sixth moments of the x_P distribution for the seven particles/decay modes used in this analysis. The listed uncertainties are statistical and systematic uncertainties.

	$\langle x_P{}^4 \rangle \times 1000$	$\langle x_P{}^5 \rangle \times 1000$	$\langle x_P{}^6 \rangle \times 1000$
$D^0 \to K^-\pi^+$	$161.83 \pm 0.25 \pm 2.19$	$116.97 \pm 0.22 \pm 1.90$	$88.08 \pm 0.19 \pm 4.77$
$D^+ \to K^-\pi^+\pi^+$	$171.54 \pm 0.24 \pm 1.28$	$125.62 \pm 0.22 \pm 1.16$	$95.52 \pm 0.19 \pm 1.11$
$D_s^+ \to \phi\pi^+$	$244.69 \pm 0.81 \pm 12.06$	$188.72 \pm 0.76 \pm 10.64$	$150.59 \pm 0.72 \pm 9.75$
$\Lambda_c^+ \to p^+K^-\pi^+$	$163.04 \pm 0.52 \pm 5.11$	$115.07 \pm 0.46 \pm 1.94$	$85.06 \pm 0.41 \pm 2.31$
$D^{*+} \to D^0\pi^+$	$211.55 \pm 0.57 \pm 5.36$	$162.26 \pm 0.53 \pm 7.05$	$128.24 \pm 0.49 \pm 8.17$
$\to D^+\pi^0$	$196.24 \pm 0.58 \pm 16.67$	$150.28 \pm 0.53 \pm 15.30$	$118.85 \pm 0.49 \pm 13.89$
$D^{*0} \to D^0\pi^0$	$215.63 \pm 0.68 \pm 12.47$	$160.05 \pm 0.59 \pm 7.98$	$126.87 \pm 0.54 \pm 8.72$

and final state radiation (ISR and FSR) as well as electro-weak corrections. 10^8 $c\bar{c}$ events were generated with $\mathcal{KK}$ and hadronised with the PYTHIA generator.

For the generated events, x_P was divided into 20 bins of equal width and a three-parameter fit to the production angle was performed:

$$f(\theta, x_P) = a_0(x_P)\left[\frac{3}{8}(1 + \cos^2\theta) + \frac{3}{4}r_S(x_P)\sin^2\theta + \frac{3}{4}r_C(x_P)\cos\theta\right] \quad (2)$$

where a_0 is the normalisation and r_S and r_C are the relative contributions for the $\sin^2\theta$ and the $\cos\theta$ terms, respectively. The results of these fits are shown in Fig. 8 as the solid line, together with the measured data points.

For data, the signal yield was determined in bins of x_P and $\cos\theta$, where θ is the production angle of the charmed hadron. It should be noted that here, the efficiency correction depends on x_P and $\cos\theta$.

x_P was divided into only 4 bins: $x_P < 0.3$, $0.3 < x_P < 0.5$, $0.5 < x_P < 0.7$ and $0.7 < x_P$. The boundaries were chosen in order to roughly equalise the number of candidates per bin. Two bins each were chosen below and above $x_P = 0.5$, which is the upper kinematic limit for hadrons from B decays.

$\cos\theta$ was divided into 20 bins. In each bin of x_P and $\cos\theta$, the efficiency corrected signal yield in the mass or mass difference distributions was fitted separately for the on-resonance and continuum samples. The same signal and background functions were used as in the fits which depended only on x_P.

In a second step, a three-parameter fit (similar to Eq. 2) to the signal yields was performed in bins of x_P. The fit range was restricted to $-0.8 < \cos\theta < 0.8$. As a systematic check, the range was tightened to $-0.7 < \cos\theta < 0.7$.

No significant deviation of the r_S and the r_C parameters from their expectation was found for the continuum sample. The expectation from the $\mathcal{KK}$ generator was of the same order as the statistical uncertainties except for the r_S term in the lowest x_P bin, where gluon radiation introduces a longitudinal momentum component and therefore smears out the initial distribution of the production angle. This smearing introduces a significant $\sin^2\theta$ term, to which the measured values in this regime agree well. As the number of entries in the low x_P bins also diminish, the statistical uncertainties increase to roughly the same size as the expected effect. The fitted values for r_S and r_C in the lowest x_P bin in the continuum samples suffer from very low statistics (see Fig. 3). For the D_s^+ and the Λ_c^+, the lowest bins in the continuum samples have been neglected as the numbers of entries in these bins were too low to perform an angular analysis.

For the on-resonance sample with higher statistics, the r_S terms significantly deviate from zero for $x_P < 0.5$, as B decays with different production angle distributions also contribute. The r_C term is again consistent with both zero and the expectation from the MC generator. Tables VIII and IX list the measured values for the r_S and r_C values for the continuum and the on-resonance data. The systematic uncertainties here include

the uncertainties discussed in the standard analysis as well as the uncertainty due to the restricted fit range.

VI. INTERPRETATION

A. Contributions from Higher Resonances

Contributions from excited states have been considered only in the x_P distributions of the D^0 and the D^+ and for these, only contributions from D^{*0} and D^{*+} were considered. For higher resonances, both production cross-section and branching fractions of *e.g.* D^{**} have large uncertainties and have been neglected. In order to reduce the statistical uncertainty, a MC-based correction was applied: Three large samples of several million MC events were generated without a detailed detector simulation. These samples were required to contain the decay modes $D^{*+} \to D^0 \pi^+$, $D^{*+} \to D^+ \pi^0$ and $D^{*0} \to D^0 \pi^0$, respectively. For these events, the x_P of the parent D^{*+}/D^{*0} vs. the x_P of the daughter D^0/D^+ were stored in a two dimensional matrix. The measured and efficiency corrected D^{*0} and D^{*+} x_P distributions were multiplied with this matrix in order to estimate the x_P distribution for all D^0's and D^+'s coming from D^{*+}/D^{*0} decays.

The two plots at the top of Fig. 9 show the contributions of D^{*+} and D^{*0} decays to the D^0 fragmentation function (left), and the contribution of D^{*+} decays to the D^+ fragmentation function (right). These plots are not corrected for the branching fraction of the D decay. The bottom plot in Fig. 9 shows primary D^0 and D^+ fragmentation spectra: the total D^0 (D^+) spectrum minus the contribution from D^{*0} and D^{*+} (D^{*+}only) decays. The difference of 13% between the sum of primary produced D^0 and D^+ should be compared to the 6.5% relative uncertainty in the $D^+ \to K^- \pi^+ \pi^+$ branching fraction. Also, as only the contribution from D^* decays has been considered, the remaining difference may be due to the contribution of other resonances. In the generic MC sample, where primary D^0's and D^+'s were produced in equal amounts, there was an excess of 6% in the

27

production of D^0 (compared to D^+) mesons in the decay of resonances other than D^{*+}.

B. Ratios

Comparisons of production rates for various particles are useful for understanding the dynamics of fragmentation, as systematic errors cancel in the ratio. In this section we present ratios of both integrated cross-sections and cross-sections as a function of x_P, to characterise general properties of fragmentation and to test the agreement between MC simulation and data.

Table X presents three ratios of total production cross sections. Since the production of D^{*+} and D^{*0} is included in the total D^+ and D^0 production rate (all D^{*+} decay to either D^+ or D^0, and all D^{*0} to D^0), the ratio of D^* to D production measures $V/(V+P)$, the probability of producing a vector charmed meson. (Here we write V for vector and P for pseudo-scalar meson production rates.) A correction is necessary to account for higher resonances decaying directly to $D^{+,0}$. For example, based on the measured production rates of the $D_1(2420)$ and $D_2^*(2460)$ [32] mesons, known branching fractions [28], and isospin relations, we find a correction of $-(3.7 \pm 3.3)\%$ to the first ratio. In principle, further corrections due to decays of broad D^{**} states and charmed-strange mesons are also required. However, no corrections have been applied to the values presented in Table X.

Similarly, the second ratio measures the production rate of charmed-strange mesons as a fraction of all charmed mesons, up to corrections for $D_{s1}(2536)$ and $D_{s2}^*(2573)$ decays. The third ratio measures the production rate of charmed baryons relative to that of charmed mesons, excluding the charmed-strange baryon states. For comparison, see [33].

Ratios of production rates as a function of x_P allow momentum-dependent effects in fragmentation to be studied, although contributions from decays of higher states also appear. Fig. 10 shows the following five ratios as a function of x_P, for both on-resonance

and continuum data:

(a) $x_P(D^{*+})/x_P(D^+_{prim})$, sensitive to the production rate of vector relative to pseudo-scalar mesons;

(b) $x_P(D^0_{prim})/x_P(D^+_{prim})$, sensitive to charged relative to neutral pseudo-scalar production;

(c) $x_P(D^+_s)/x_P(D^+_{prim})$, sensitive to the production of strange quarks;

(d) $x_P(\Lambda^+_c)/x_P(D^+_{prim})$, sensitive to the production of baryons relative to mesons;

(e) $x_P(D^{*0})/x_P(D^{*+})$, the relative production rate of the vector mesons.

The suffix "prim" denotes x_P distributions corrected for the contributions from D^* decays; D^+ production has been chosen as the denominator in (a)–(d), as this correction is smaller than that for D^0. No other corrections for excited states have been applied.

The production ratios in Fig. 10(a) and (b) are similar for on-resonance and continuum data. In Fig. 10(c), the contribution of B meson decays to D^+_s production can be clearly seen in the low-x_P region. In Fig. 10(d), baryon production in B decays is seen to be suppressed below $x_P \approx 0.4$. As x_P approaches unity, the Λ^+_c/D^+ production ratio goes to zero, consistent with the conservation of baryon number.

Four similar ratios are shown in Fig. 11(a)–(d) for both continuum data (full squares) and MC simulations, to test the performance of the MC for various fragmentation function parameters. In these plots, the total D^+ production rate, without D^* subtraction, is used in the denominator of the ratios. The open histograms show the generic MC sample, which agrees with the data only for the highest values of x_P of the distributions in Fig. 11(a) and (b), but fails to describe the data distributions at lower values. The open squares show a second MC sample generated with the Bowler fragmentation function, which shows a similar behaviour.

Noting that the parameter **PARJ(13)** in PYTHIA gives the probability for a charmed hadron produced in fragmentation to have spin one, 50 MC samples of 10^7 events each were generated, with **PARJ(13)** values ranging from 0.25 to the default value 0.75 given by spin counting. These samples were generated in addition to the "reweighted samples" used for more refined MC comparisons as described in the next section. A reduced chi-squared $\tilde{\chi}^2$ was calculated for these samples and the measured and corrected ratios, and a fourth-order polynomial in **PARJ(13)** was fitted to the results. The minimum $\tilde{\chi}^2$ was found to occur at **PARJ(13)** $= 0.592 \pm 0.021$ for the $x_P(D^{*+})/x_P(D^+)$ ratio, and 0.592 ± 0.046 for the $x_P(D^0)/x_P(D^+)$ ratio, where the uncertainties denote the 1σ range in the fitted polynomial. We note that models of hadron production more sophisticated than spin counting predict values for **PARJ(13)** below 0.75; see [34] and references therein.

In Fig. 11(a)–(d) a third MC sample generated with the Bowler fragmentation function, and **PARJ(13)** $= 0.59$, is shown with closed triangles. This sample and the data agree well within the error bars over almost the entire range in Fig. 11(a) and (b). All three MC samples fail to describe the ratios in Fig. 11(c) and (d): both the endpoints and the shape disagree. The difference between the MC samples is small compared to the discrepancy with data for D_s^+/D^+ production in Fig. 11(c); while Bowler fragmentation (open squares and triangles) gives an improved description of Λ_c^+/D^+ production in Fig. 11(d), the agreement is still poor. There are no obvious parameters in the MC which can affect these two ratios in such a way as to improve the agreement between data and MC.

C.   Comparison of x_P distributions with predictions from MC generators

The models used by MC generators are based on simplified assumptions and require input from experiment: this is reflected in the models' input parameters. The commonly used JETSET/PYTHIA generators are based on the Lund or string model, in which a coloured string is expanded between two emerging partons. The energy stored in the

30

string increases with increasing distance, and eventually allows the production of a new quark anti-quark pair. The quark (anti-quark) then produces a meson together with the initial anti-quark (quark). The energy distribution of the new quark or anti-quark is described by a fragmentation function. Various fragmentation function models have been published; see Table XI for a summary. These models depend upon up to two independent variables, these are the transverse mass $m_\perp = \sqrt{m^2 + p_\perp^2}$ of the newly created hadron, and z, the fraction of the longitudinal energy $E + p_\parallel$ which the meson inherits from the initial quark.

Not all models listed in Table XI are implemented in the JETSET/PYTHIA generator. In order to be able to compare all models to data, a reweighting technique has been applied. Here, several million events referred to as "reweighted samples" have been generated, allowing a more elaborate comparison than described in Section VI B. For these events, z and $p_\perp$ were stored together with the event. This allowed each event to be reweighted in order to mimic any other fragmentation function. Scans through the parameter space of the five listed fragmentation functions have been performed on these special samples. This analysis was performed on five different hadrons; $D^{*0} \to D^0 \pi^0$ and $D^{*+} \to D^+ \pi^0$ have been omitted because of the large systematic uncertainty due to the detection efficiency of the slow neutral pion.

For data and MC, the x_P distributions were compared using uncorrected data and the reweighted special MC samples after full detector simulation. A χ^2 was calculated based upon the distribution of the reweighted special sample and the measured data distribution. Only statistical uncertainties in each x_P bin were taken into account and only bins which contained entries in data or MC were included. The number of bins minus the number of parameters of the fragmentation function was used as the number of degrees of freedom

31

($d.o.f.$). The weights in the reweighting procedure were constructed in such a way that the number of events before and after reweighting stayed constant. This way the total value of the χ^2 becomes dependent on the size of the data and MC samples; the relative χ^2 values, however, allow a direct comparison between the different fragmentation functions.

Table XII shows the $\chi^2_{min}/d.o.f.$ for all five particles and five fragmentation functions. For all five particles a similar trend is visible. The Bowler model in general agrees best with the data. The Lund models shows a similar performance in describing the spectra, its $\chi^2_{min}/d.o.f.$ being by factors of 2–3 better than the next best model. For D^+ and D^{*+} the $\chi^2_{min}/d.o.f.$ is slightly worse than for the Bowler model. In the minimum of the $\chi^2/d.o.f.$ distributions the a parameter deviates strongly from the default for most of the particles. As the Lund model is employed for fragmentation of all flavour species, such a large change in the parameter would also change the particle spectrum of light mesons. Therefore, further tuning of the second parameter to the Lund fragmentation function has been omitted.

The models by Collins and Spiller and by Kartvelishvili show a similar χ^2_{min} for all particles, about factors of two to three worse than that of the best models. The last model, that of Peterson, shows the worst agreement with a reduced χ^2_{min} of 15 and well above, ruling out this model for describing data at this CME.

The input parameters for the fragmentation functions at the minimum of the $\chi^2/d.o.f.$ distributions are listed in Table XIII.

In summary, the Bowler model shows the best agreement between data and MC, however, large differences are still present. These differences might be resolved by adjusting other parameters of the generators as well, but such a task is out of scope for this analysis. The Lund model shows the second best agreement. The models by Kartvelishvili and by Collins and Spiller show larger deviations and the commonly used model by Peterson shows the worst agreement between data and MC.

VII. SUMMARY

A new determination of the charm fragmentation function at a CME close to the $\Upsilon(4S)$ resonance has been presented. The measured x_P spectra have been compared to those of five different parametrisations in MC via a reweighting procedure, and the best input parameters have been found. The best agreement between data and MC has been found for the Bowler model and the Lund model. Additionally, the peak positions and the first six moments of the x_P distributions have been measured. These measurements will allow detailed comparisons between experiment and theory. The total production cross-section, as well as x_P dependent ratios of the fragmentation functions, place stringent tests on existing MC generators, which so far completely fail to describe the x_P dependent ratios of $x_P(D_s^+)/x_P(D^+)$ and $x_P(\Lambda_c^+)/x_P(D^+)$. For the first time, the production rates of D^+ and D^0 excluding the decay of D^* mesons have been measured. They were found to agree reasonably well with each other.

The efficiency corrected data points will be made available via download in the Durham HEP REACTION DATA DataBase [35]. It is presented in a different way as shown this article. Separate sets of the continuum and the on-resonance samples are given as $sBd\sigma/dx_P$, *i.e.* scaled by the nominal center-of-mass energies of 10.52 GeV and 10.58 GeV, respectively, and not corrected for the branching ratios. The on-resonance data includes the additional correction for ISR of $+0.27\%$, see Section III for details.

[1] OPAL Coll., G. Abbiendi *et al.*: Eur. Phys. J. **C17**, 19 (2000).

[2] G. Altarelli, G. Parisi: Nucl. Phys. **B126**, 298 (1977);

L.N. Lipatov: Sov. J. Nucl. Phys. **20**, 94 (1975);

V.N. Gribov, L.N. Lipatov: Sov. J. Nucl. Phys. **15**, 43 (1972);

Yu.L. Dokshitzer: Sov. Phys. JETP **46**, 641 (1977).

[3] T. Sjöstrand: Comput. Phys. Comm. **82**, 74 (1994).

[4] T. Sjöstrand *et al.*: Comput. Phys. Comm. **135**, 238 (2001).

[5] G. Corcella *et al.*: JHEP **0101**, 010 (2001), hep-ph/0210213;

G. Marchesini *et al.*: Comput. Phys. Comm. **67**, 465 (1992).

[6] Aleph Coll., A. Heister *et al.*: Phys. Lett. **B512**, 30 (2001).

[7] Delphi Coll., P. Abreu *et al.*: Z. Phys. **C66**, 323 (1995).

[8] OPAL Coll., G. Abbiendi *et al.*: Euro. Phys. J **C29**, 463 (2003).

[9] SLD Coll., K. Abe *et al.*: Phys. Rev. **D65**, 092006 (2002).

[10] Aleph Coll., R. Barate *et al.*: Euro. Phys. J. **C16**, 597 (2000).

[11] OPAL Collab., R. Akers *et al.*: Z. Phys. **C67**, 27 (1995).

34

[12] C. Peterson, D. Schlatter, I. Schmitt, P.M. Zerwas: Phys. Rev. **D27**, 105 (1983).

[13] V.G. Kartvelishvili, A.K. Likhoded, V.A. Petrov: Phys. Lett. **B78**, 615 (1978).

[14] P.D.B. Collins, T.P. Spiller: J. Phys. **G11**, 1289 (1985).

[15] B. Andersson, G. Gustafson, B. Söderberg: Z. Phys. **C20**, 317 (1983).

[16] M.G. Bowler: Z. Phys. **C11**, 169 (1981).

[17] CLEO Coll., M. Artuso *et al.*: Phys. Rev. **D70** , 112001 (2004).

[18] CLEO Coll., D. Bortoletto *et al.*: Phys. Rev. **D37**, 1719 (1988);
Erratum ibid. D39, 1471 (1989).

[19] ARGUS Coll., H. Albrecht *et al.*: Z. Phys. **C52**, 353 (1991).

[20] O. Biebel, P. Nason, and B.R. Webber: hep-ph/0109282;
extended version of [28].

[21] S. Kurokawa, E. Kikutani: Nucl. Inst. Meth. **A499**, 1 (2003);
and other papers included in this Volume.

[22] Belle Coll., A. Abashian *et al.*: Nucl. Inst. Meth. **A479**, 117 (2002).

[23] Belle Coll., K.Abe *et al.*: Phys. Rev. **D64**, 072001 (2001).

[24] see http://www.lns.cornell.edu/public/CLEO/soft/QQ.

[25] R. Brun *et al.*, GEANT 3.21, CERN Report DD/EE/84-1, 1984.

[26] see http://www.slac.stanford.edu/~lange/EvtGen

[27] A. Hoecker, V. Kartvelishvili: Nucl. Inst. Meth. **A372**, 469 (1996).

[28] S. Eidelman *et al.*: Phys. Lett. **B592**, 1 (2004).

[29] Belle Coll., T. Uglov *et al.*: Phys. Rev. **D70**, 071101 (2004).

[30] BaBar Coll., B. Aubert *et al.*: Phys. Rev. **D65**, 091104 (2002).

[31] S. Jadach, B.F.L. Ward and Z. Wąs: Phys. Rev. **D63**, 113009 (2001);
S. Jadach, B.F.L. Ward and Z. Wąs: Comput. Phys. Comm. **130**, 260 (2000);
S. Jadach, B.F.L. Ward and Z. Wąs: Phys. Lett. **B449**, 97 (1999).

[32] CLEO Coll., P. Avery *et al.*: Phys. Rev. **D41**, 774 (1990).

[33] L. Gladilin: hep-ex/9912064.

[34] K. Cheung: *Recent Progress on Perturbative QCD Fragmentation Functions,* Proceedings of the 1995 PASCOS/Hopkins Workshop, Baltimore, or hep-ph/9505365;

E. Braaten, K. Cheung, S. Fleming, and T.C. Yuan: Phys. Rev. **D51**, 4819 (1995);

Phys. Rev. **D48**, 5181 (1993);

M. Suzuki: Phys. Rev. **D33**, 676 (1986);

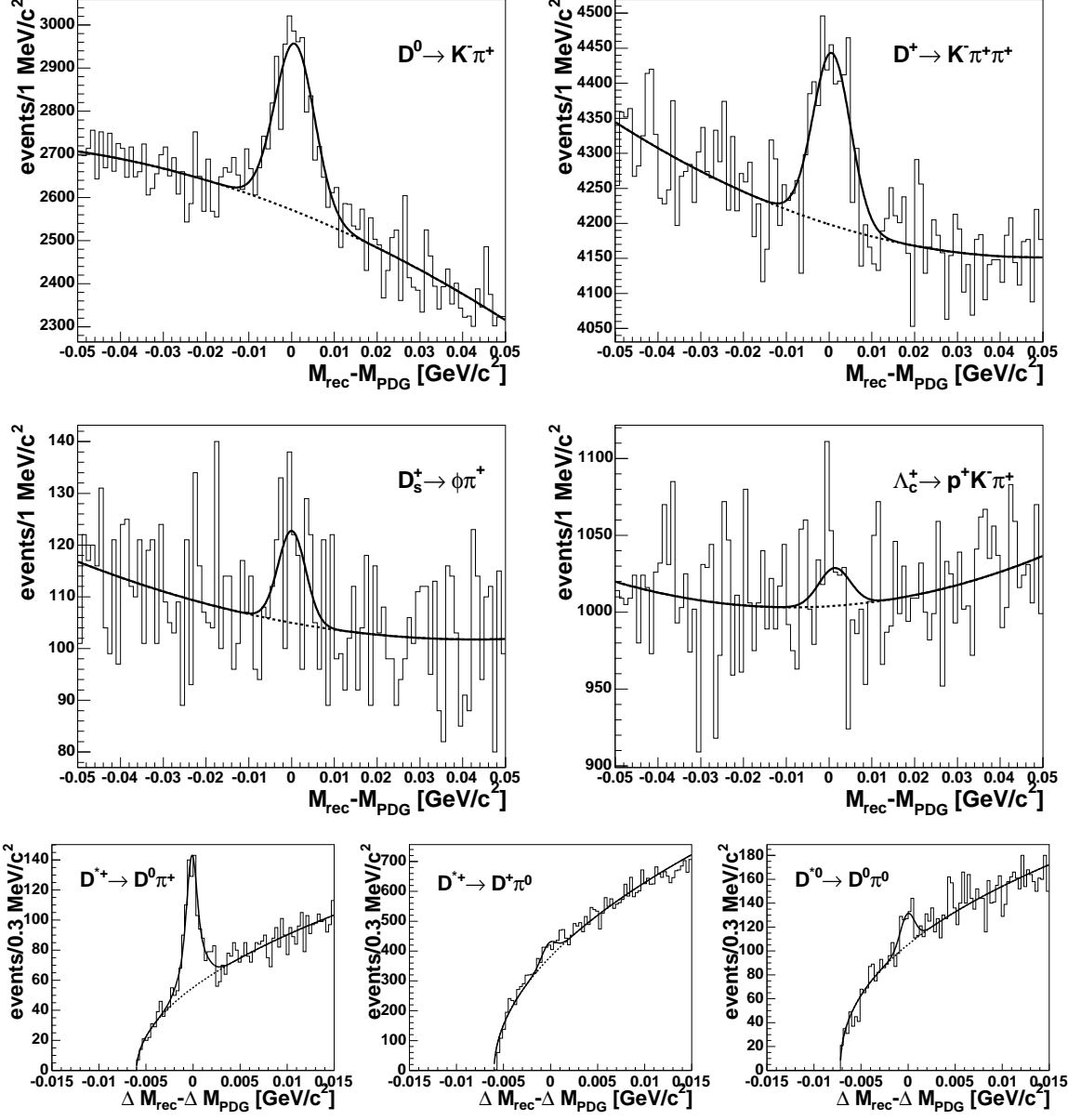R. Suaya, J.S. Townsend: Phys. Rev. **D19**, 1414 (1979).

[35] http://durpdg.dur.ac.uk/HEPDATA/

FIG. 1: Mass and mass difference distributions for all charmed hadrons reconstructed in this analysis, for $0.28 < x_P < 0.30$ for the continuum sample. The histograms show the data, the dotted line describes only the background, the full line includes the signal. The top row shows the D^0 (left) and the D^+ (right), the middle shows the D_s^+ (left) and the Λ_c^+ (right), and the bottom row shows $D^{*+} \to D^0\pi^+$ (left), the alternative decay mode $D^{*+} \to D^+\pi^0$ (middle), and the D^{*0} (right).
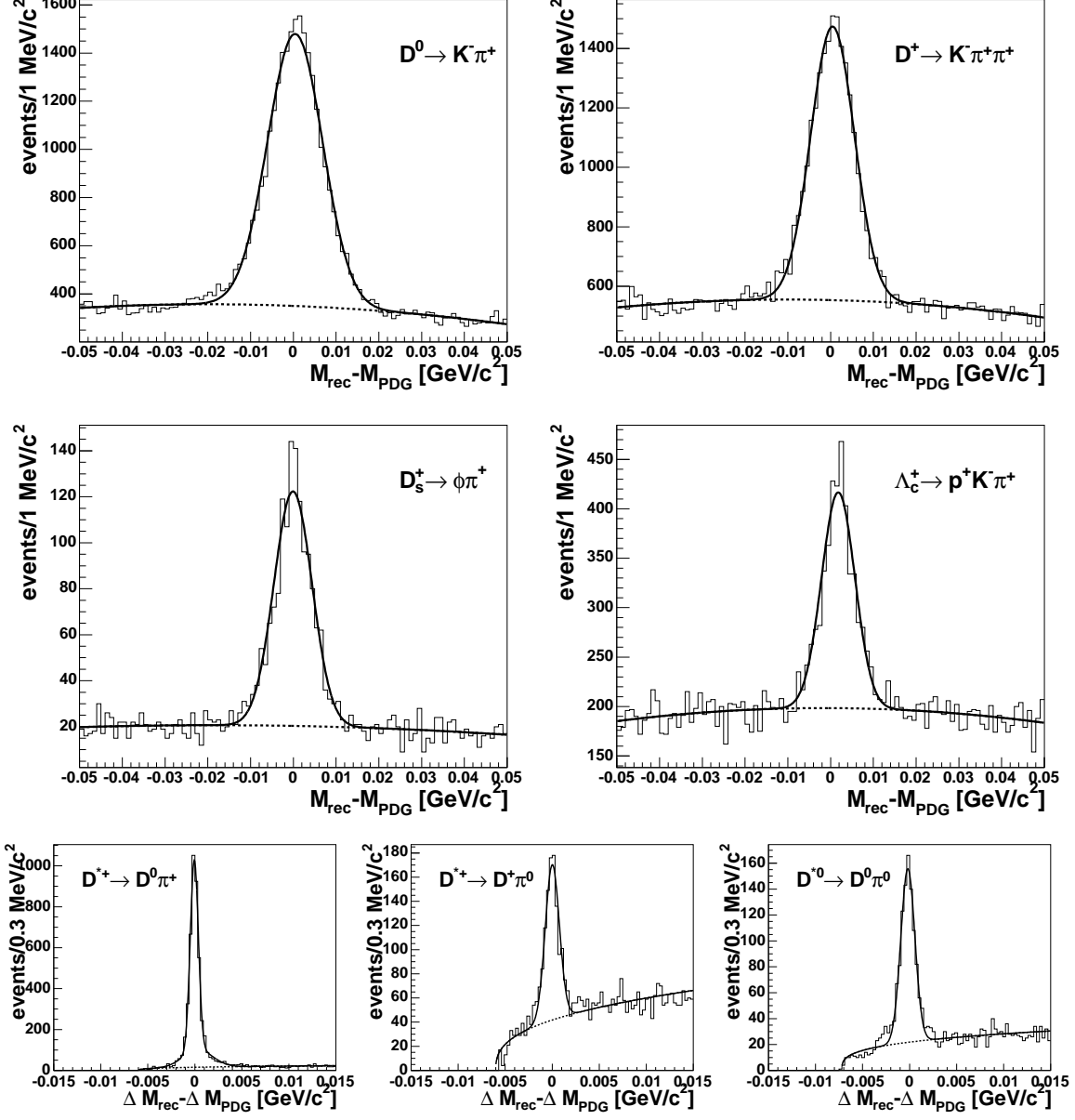
37

FIG. 2: Mass and mass difference distributions for all charmed hadrons reconstructed in this analysis, for $0.68 < x_P < 0.70$. The order of the plots is the same as in Fig. 1. As in the previous figure, the histograms show the data, the dotted lines describe only the background, the full lines include the signal.
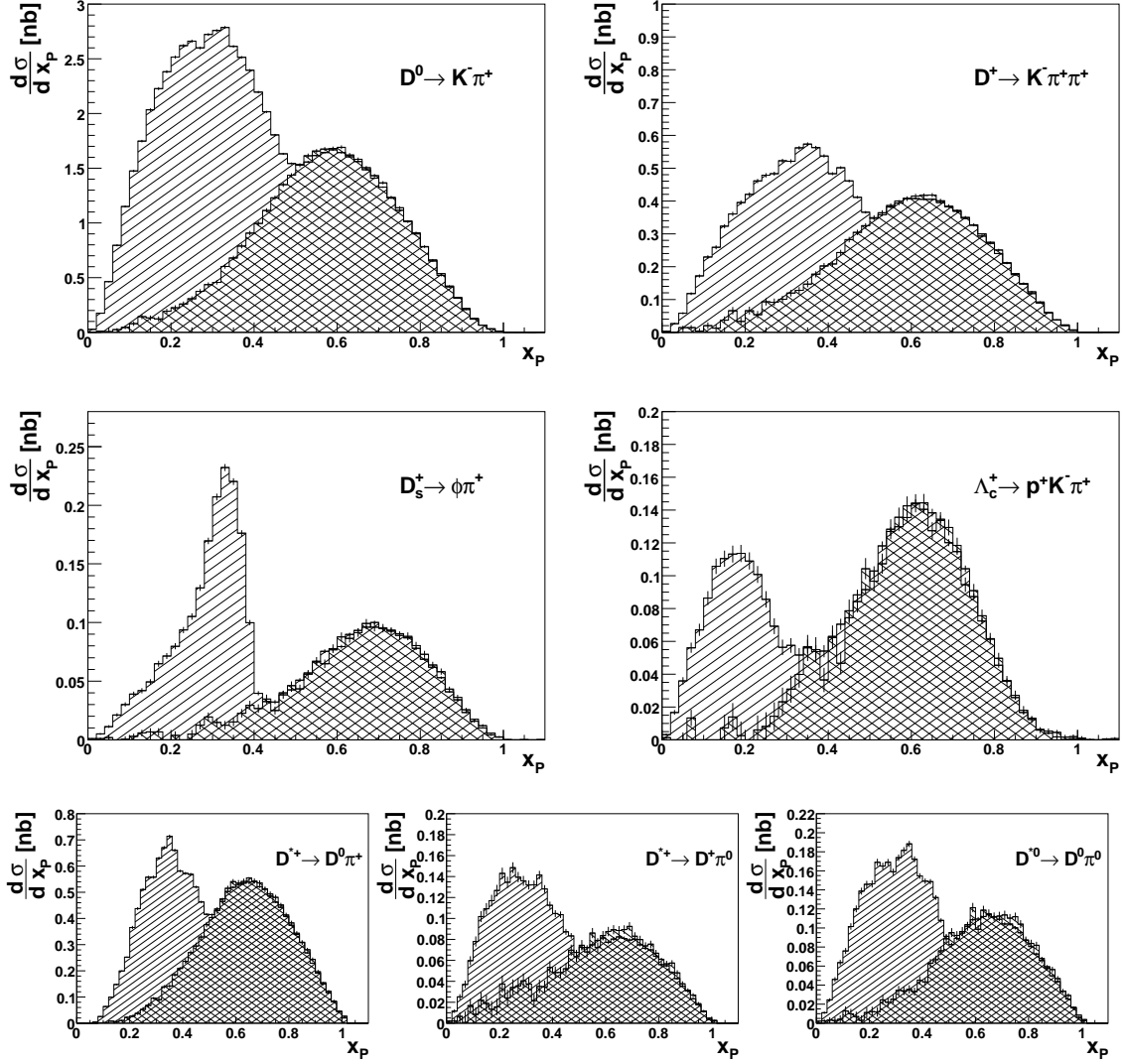
FIG. 3: The signal yield not corrected for efficiencies for the charmed hadrons. The order of the particles is the same as in Fig. 1. The contribution from B decays in the on-resonance samples (down-left hatching) is clearly visible in the region $x_P < 0.5$. The error bars show the statistical uncertainties only.
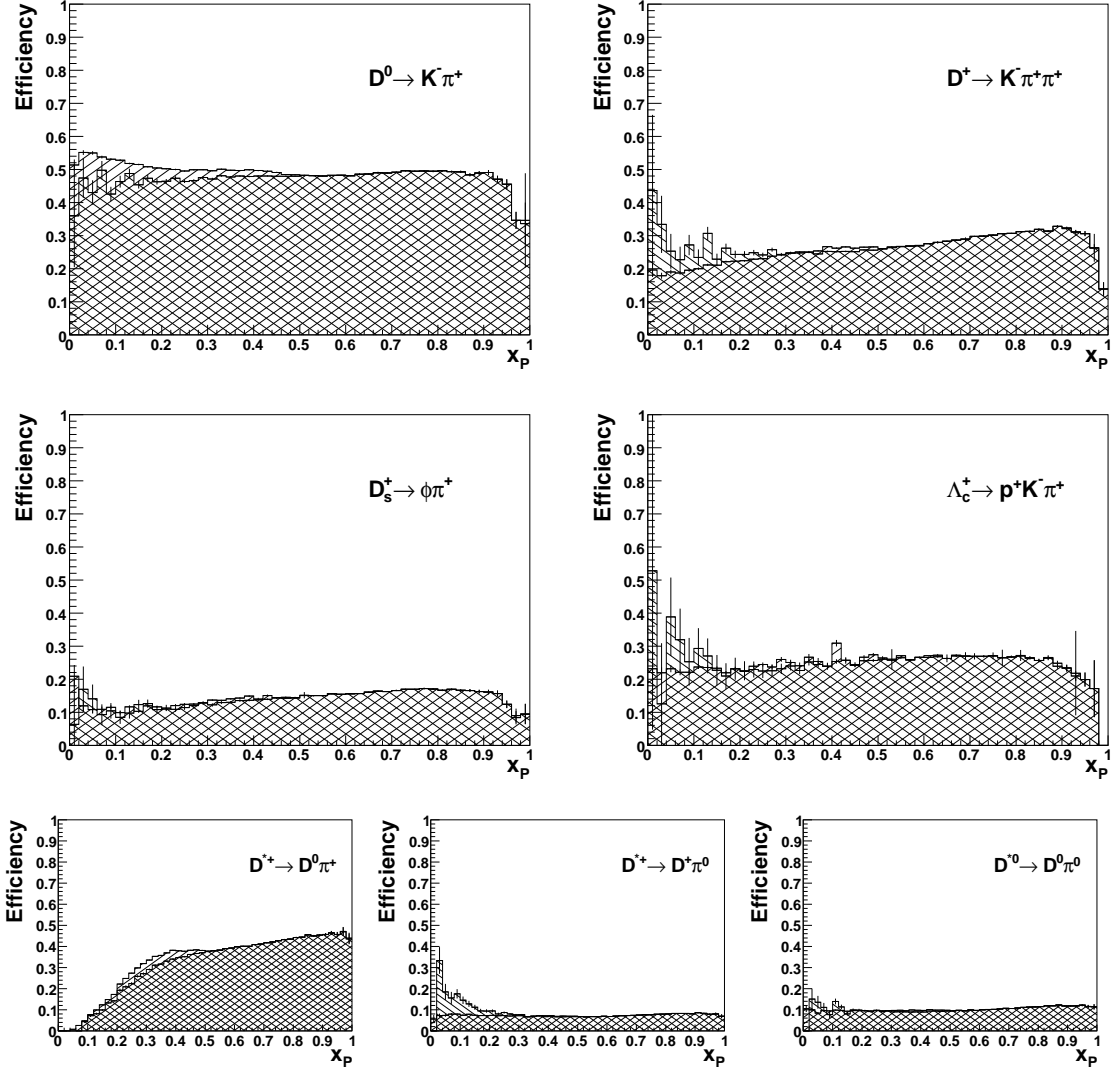
FIG. 4: The efficiencies for the charmed hadrons used in this analysis. The order of the particles is the same as in Fig. 1. The different production angle distributions for the on-resonance (down-left hatching) and the continuum sample (down-right hatching) result in different efficiencies for these samples. The error bars show the statistical uncertainties only.
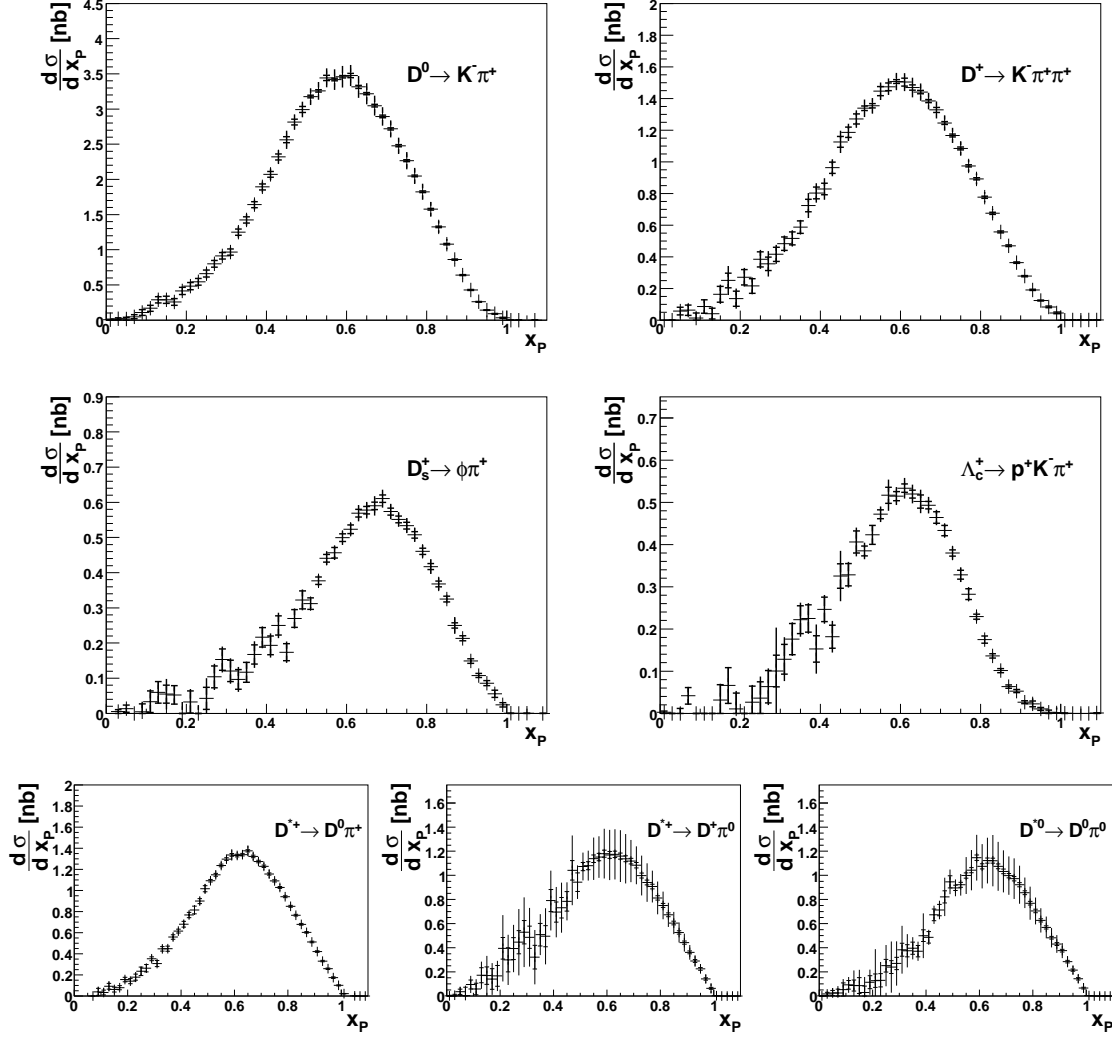
40

FIG. 5: Efficiency corrected momentum distributions for the charmed hadrons produced in e^+e^--annihilation events, i.e. from fragmentation of charm quarks. The order of the particles is the same as in Fig. 1. For $x_P > 0.5$, the on-resonance and continuum data have been combined by a weighted average. The inner error bars show the statistical, the outer error bars the total uncertainties.
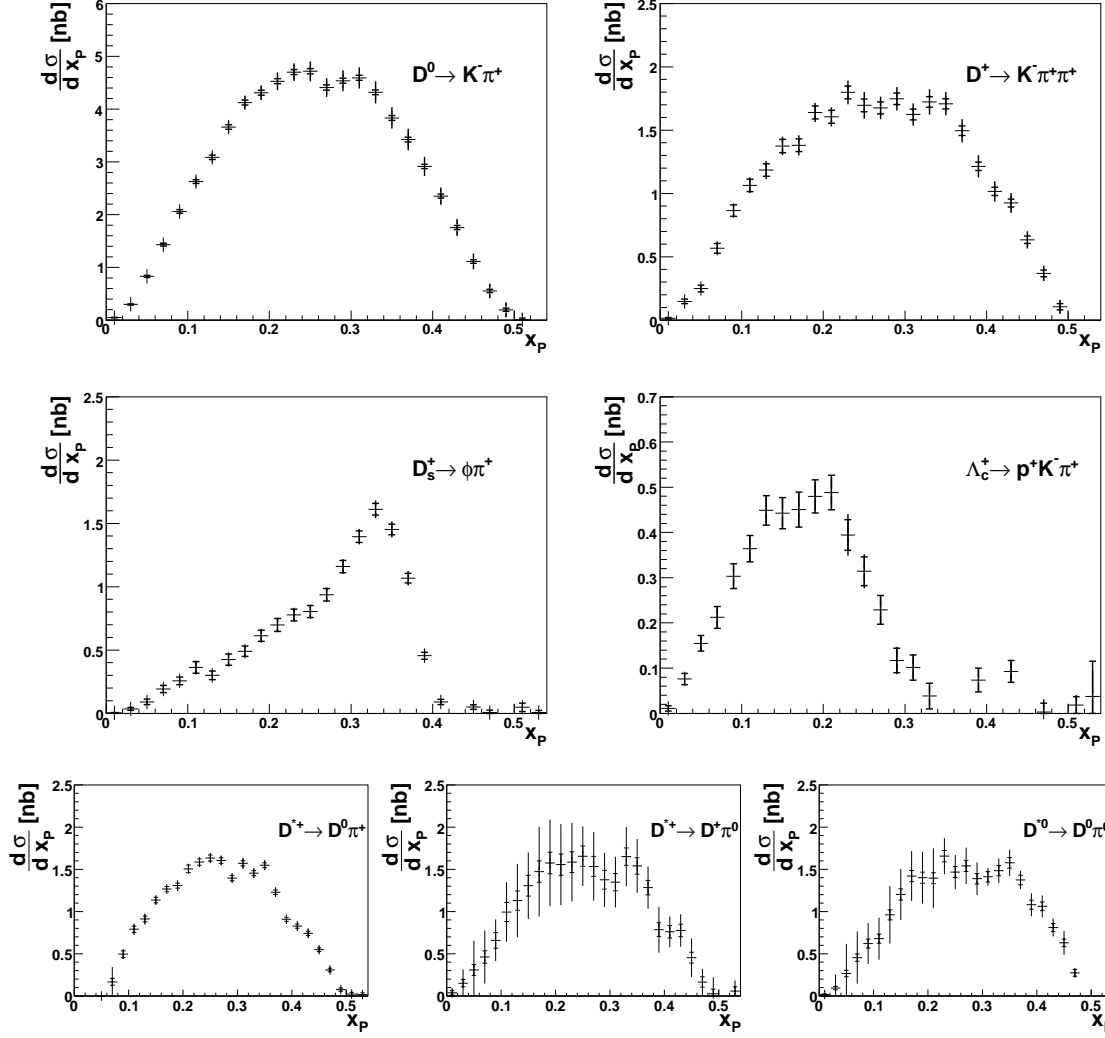
41

FIG. 6: Efficiency corrected and continuum subtracted momentum distributions for the charmed hadrons from B decays used in this analysis. The x_P range is restricted to $x_P < 0.55$. The order of the particles is the same as in Fig. 1. The inner error bars show the statistical, the outer error bars the total uncertainties.
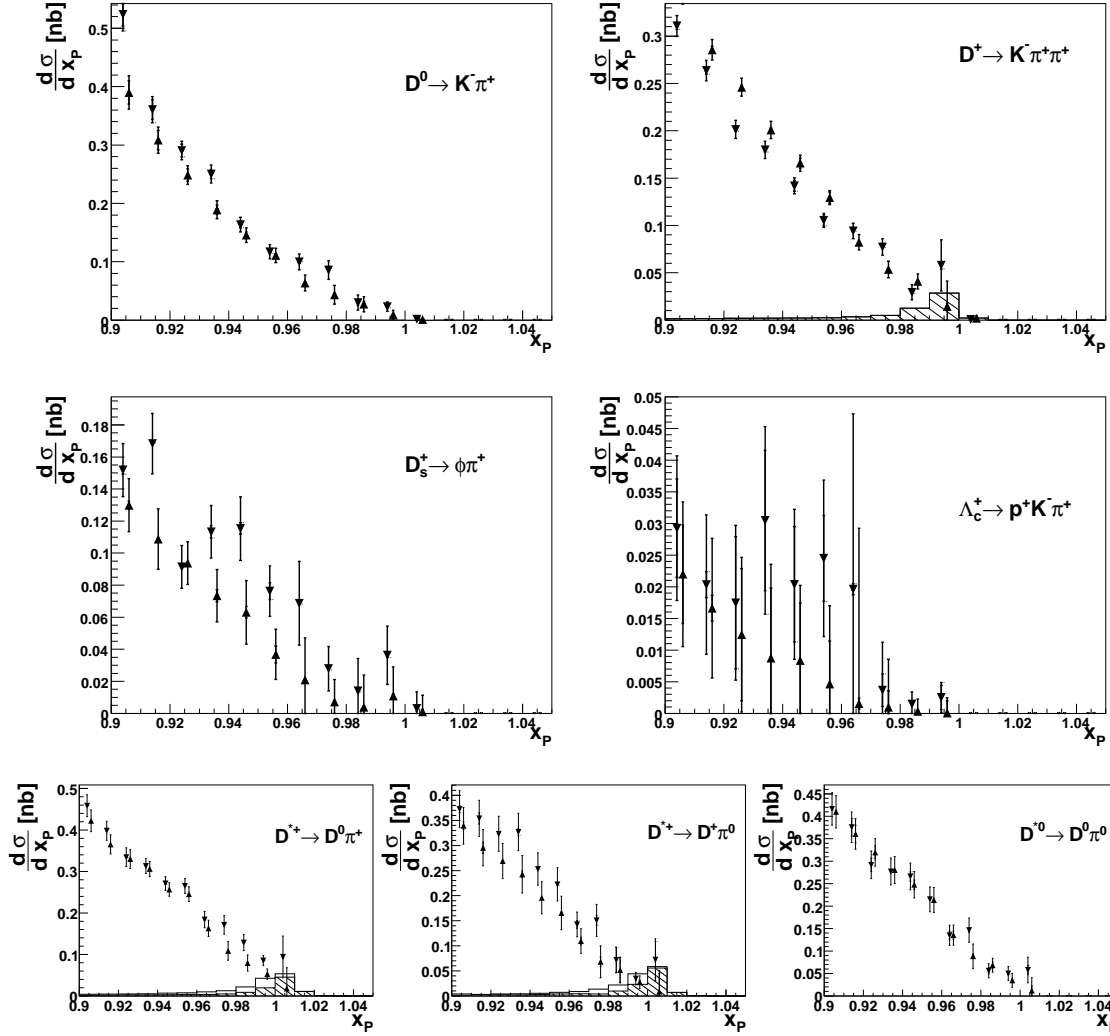
FIG. 7: An expanded view of the high x_P region. The downward (upward) triangles show the efficiency-corrected (unfolded) histograms. Events above the naive limit of $x_P = 1$ can be produced via $e^+e^- \to D^{*+}D^{(*)}$; this is shown in the D^{*+} x_P distributions as a hatched (open) histogram for $e^+e^- \to D^{*+}D^-$ (sum of $e^+e^- \to D^{*+}D^-$ and $e^+e^- \to D^{*+}D^{*-}$). The order of the particles is the same as in Fig. 1. The inner (outer) error bars show the statistical (total) uncertainties.
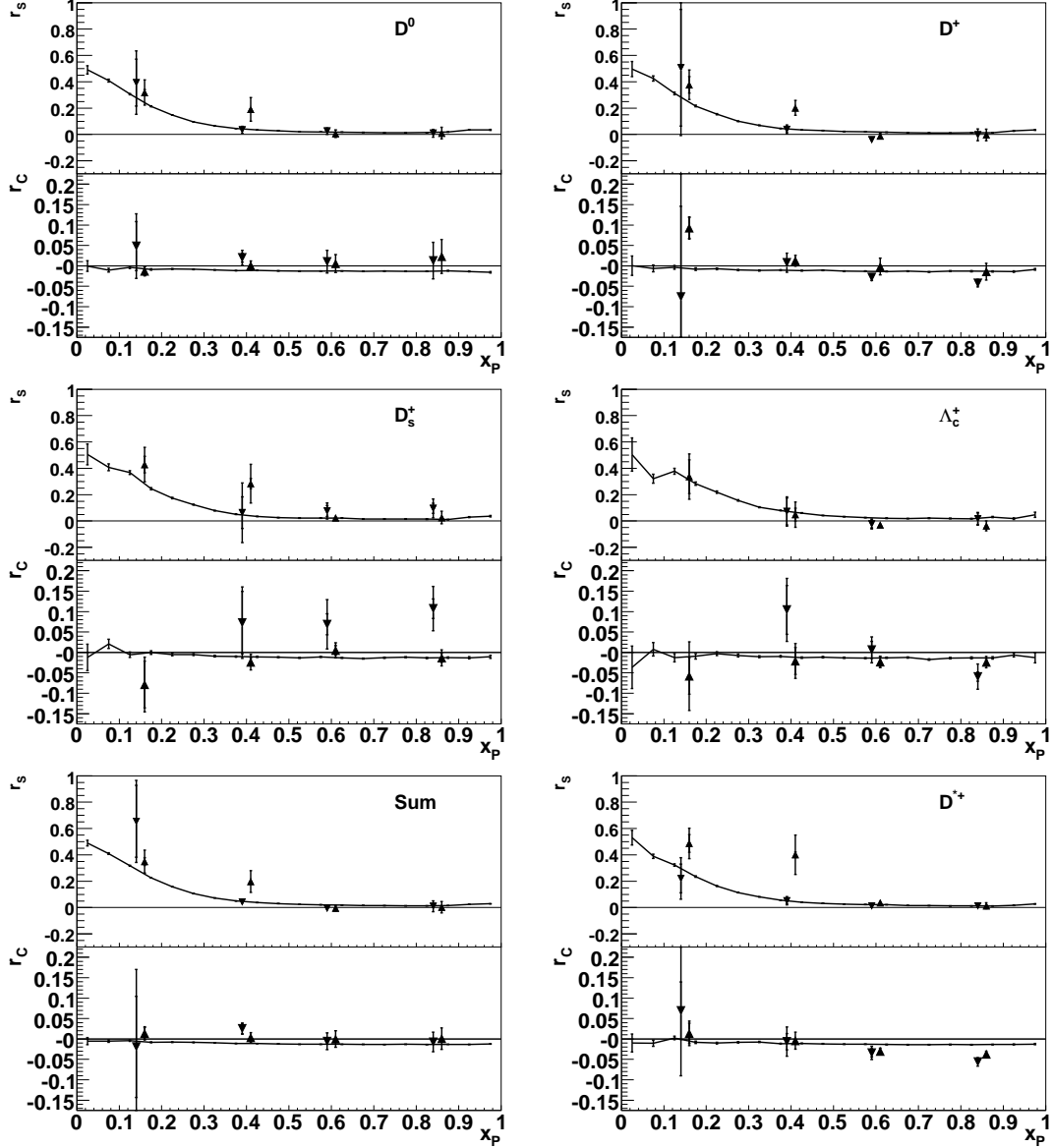
43

FIG. 8: The production angle coefficients r_S (upper distributions) and r_C (lower distributions) for the four ground state charmed hadrons: D^0 and D^+ at the top, D_s^+ and Λ_c^+ in the middle. The sum of all ground states after efficiency correction and an excited D state ($D^{*+} \to D^0\pi^+$) are shown at the bottom. The upwards (downwards) triangles show on-resonance (continuum) data. The connected points show the results from the $\mathcal{KK}$ generator. For display purposes, the points are slightly separated in x_P.

44

TABLE VIII: The coefficients in front of the sine-squared term (r_S) and the cosine term (r_C) for different x_P bins in the continuum sample.

particle	range in x_P	r_S	r_C
D^0	0.0 - 0.3	$0.393 \pm 0.178 \pm 0.166$	$0.048 \pm 0.079 \pm 0.008$
	0.3 - 0.5	$0.035 \pm 0.016 \pm 0.007$	$0.020 \pm 0.011 \pm 0.003$
	0.5 - 0.7	$0.025 \pm 0.008 \pm 0.014$	$0.010 \pm 0.006 \pm 0.001$
	0.7 - 1.0	$0.009 \pm 0.010 \pm 0.004$	$0.013 \pm 0.007 \pm 0.009$
D^+	0.0 - 0.3	$0.507 \pm 0.443 \pm 0.349$	$-0.076 \pm 0.222 \pm 0.005$
	0.3 - 0.5	$0.039 \pm 0.034 \pm 0.008$	$0.008 \pm 0.024 \pm 0.002$
	0.5 - 0.7	$-0.040 \pm 0.011 \pm 0.006$	$-0.028 \pm 0.008 \pm 0.004$
	0.7 - 1.0	$-0.003 \pm 0.012 \pm 0.019$	$-0.042 \pm 0.008 \pm 0.010$
D_s^+	0.3 - 0.5	$0.063 \pm 0.120 \pm 0.013$	$0.073 \pm 0.077 \pm 0.029$
	0.5 - 0.7	$0.076 \pm 0.041 \pm 0.004$	$0.069 \pm 0.026 \pm 0.007$
	0.7 - 1.0	$0.096 \pm 0.038 \pm 0.027$	$0.107 \pm 0.024 \pm 0.017$
Λ_c^+	0.3 - 0.5	$0.072 \pm 0.112 \pm 0.027$	$0.104 \pm 0.077 \pm 0.066$
	0.5 - 0.7	$-0.023 \pm 0.029 \pm 0.042$	$0.006 \pm 0.021 \pm 0.004$
	0.7 - 1.0	$0.016 \pm 0.048 \pm 0.037$	$-0.059 \pm 0.031 \pm 0.010$
Sum	0.0 - 0.3	$0.654 \pm 0.312 \pm 0.142$	$-0.019 \pm 0.124 \pm 0.039$
of	0.3 - 0.5	$0.042 \pm 0.019 \pm 0.007$	$0.025 \pm 0.013 \pm 0.008$
ground	0.5 - 0.7	$-0.007 \pm 0.007 \pm 0.011$	$-0.006 \pm 0.005 \pm 0.002$
states	0.7 - 1.0	$0.010 \pm 0.008 \pm 0.007$	$-0.007 \pm 0.005 \pm 0.008$
D^{*+}	0.0 - 0.3	$0.221 \pm 0.157 \pm 0.779$	$0.069 \pm 0.070 \pm 0.333$
	0.3 - 0.5	$0.051 \pm 0.031 \pm 0.035$	$-0.007 \pm 0.020 \pm 0.017$
	0.5 - 0.7	$0.011 \pm 0.014 \pm 0.013$	$-0.034 \pm 0.010 \pm 0.005$
	0.7 - 1.0	$0.011 \pm 0.015 \pm 0.012$	$-0.056 \pm 0.010 \pm 0.004$

TABLE IX: The same as in Table VIII, but now for the on-resonance sample.

| particle	range in x_P	r_S	r_C
D^0	0.0 - 0.3	$0.318 \pm 0.023 \pm 0.022$	$-0.013 \pm 0.011 \pm 0.008$
	0.3 - 0.5	$0.191 \pm 0.007 \pm 0.016$	$0.001 \pm 0.004 \pm 0.004$
	0.5 - 0.7	$0.005 \pm 0.004 \pm 0.004$	$0.006 \pm 0.003 \pm 0.002$
	0.7 - 1.0	$0.010 \pm 0.005 \pm 0.010$	$0.023 \pm 0.004 \pm 0.006$
D^+	0.0 - 0.3	$0.377 \pm 0.063 \pm 0.026$	$0.093 \pm 0.027 \pm 0.016$
	0.3 - 0.5	$0.202 \pm 0.015 \pm 0.008$	$0.012 \pm 0.008 \pm 0.001$
	0.5 - 0.7	$-0.011 \pm 0.006 \pm 0.005$	$-0.002 \pm 0.004 \pm 0.001$
	0.7 - 1.0	$-0.003 \pm 0.006 \pm 0.007$	$-0.014 \pm 0.004 \pm 0.001$
D_s^+	0.0 - 0.3	$0.428 \pm 0.130 \pm 0.032$	$-0.079 \pm 0.057 \pm 0.030$
	0.3 - 0.5	$0.284 \pm 0.038 \pm 0.011$	$-0.024 \pm 0.019 \pm 0.005$
	0.5 - 0.7	$0.025 \pm 0.017 \pm 0.008$	$0.005 \pm 0.011 \pm 0.001$
	0.7 - 1.0	$0.026 \pm 0.017 \pm 0.008$	$-0.013 \pm 0.011 \pm 0.008$
Λ_c^+	0.0 - 0.3	$0.336 \pm 0.172 \pm 0.044$	$-0.058 \pm 0.084 \pm 0.009$
	0.3 - 0.5	$0.048 \pm 0.049 \pm 0.027$	$-0.021 \pm 0.033 \pm 0.020$
	0.5 - 0.7	$-0.030 \pm 0.014 \pm 0.015$	$-0.023 \pm 0.010 \pm 0.003$
	0.7 - 1.0	$-0.037 \pm 0.020 \pm 0.002$	$-0.024 \pm 0.014 \pm 0.004$
Sum	0.0 - 0.3	$0.349 \pm 0.030 \pm 0.001$	$0.014 \pm 0.014 \pm 0.012$
of	0.3 - 0.5	$0.197 \pm 0.008 \pm 0.013$	$0.004 \pm 0.005 \pm 0.001$
ground	0.5 - 0.7	$-0.004 \pm 0.004 \pm 0.001$	$-0.000 \pm 0.002 \pm 0.001$
states	0.7 - 1.0	$0.002 \pm 0.004 \pm 0.006$	$0.001 \pm 0.003 \pm 0.003$
D^{*+}	0.0 - 0.3	$0.487 \pm 0.067 \pm 0.049$	$0.014 \pm 0.030 \pm 0.012$
	0.3 - 0.5	$0.401 \pm 0.021 \pm 0.004$	$-0.004 \pm 0.010 \pm 0.008$
	0.5 - 0.7	$0.037 \pm 0.008 \pm 0.002$	$-0.030 \pm 0.005 \pm 0.001$
	0.7 - 1.0	$0.014 \pm 0.008 \pm 0.001$	$-0.037 \pm 0.005 \pm 0.004$
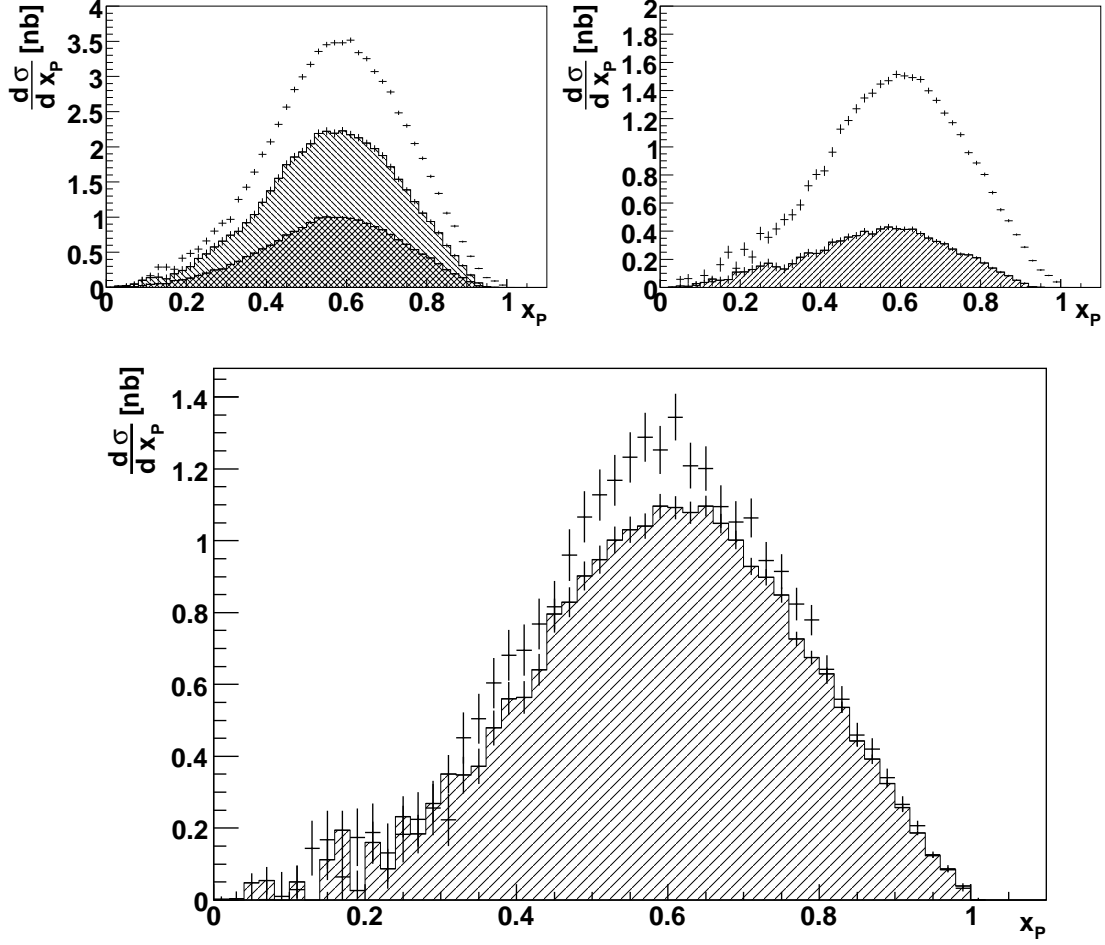
FIG. 9: Upper plots: The contributions from D^{*+} (up-right hatching) and D^{*0} (up-left hatching) decays to the D^0 (left) and D^+ (right) x_P distributions. These plots are not corrected for the branching fraction of the D decay. Lower plot: The x_P distributions for primarily produced D^0 (error bars) and D^+ (up-right hatching) mesons. Note that only contributions from D^{*+} and D^{*0} decays have been considered; the exclusion of higher resonance contributions can partially account for the differences in the x_P distributions of the D^0 and D^+. Only statistical uncertainties are shown.

TABLE X: Three ratios of total cross sections, each of the form $\sigma(e^+e^- \to AX)/\sigma(e^+e^- \to BY)$ for the continuum sample. The denominators of all ratios contain the contribution from $D^* \to D$ and other decays. For comparison, see [33]

A	B	ratio
$D^{*0} + D^{*+}$	$D^+ + D^0$	$0.527 \pm 0.013 \pm 0.024$
D_s^+	$D_s^+ + D^+ + D^0$	$0.099 \pm 0.003 \pm 0.002$
Λ_c^+	$D_s^+ + D^+ + D^0$	$0.081 \pm 0.002 \pm 0.003$

TABLE XI: The functional form of the fragmentation functions used in this analysis. The normalisation N is different for all functions. The models by Collins and Spiller and by Kartvelishvili are not included in the JETSET/PYTHIA generator.

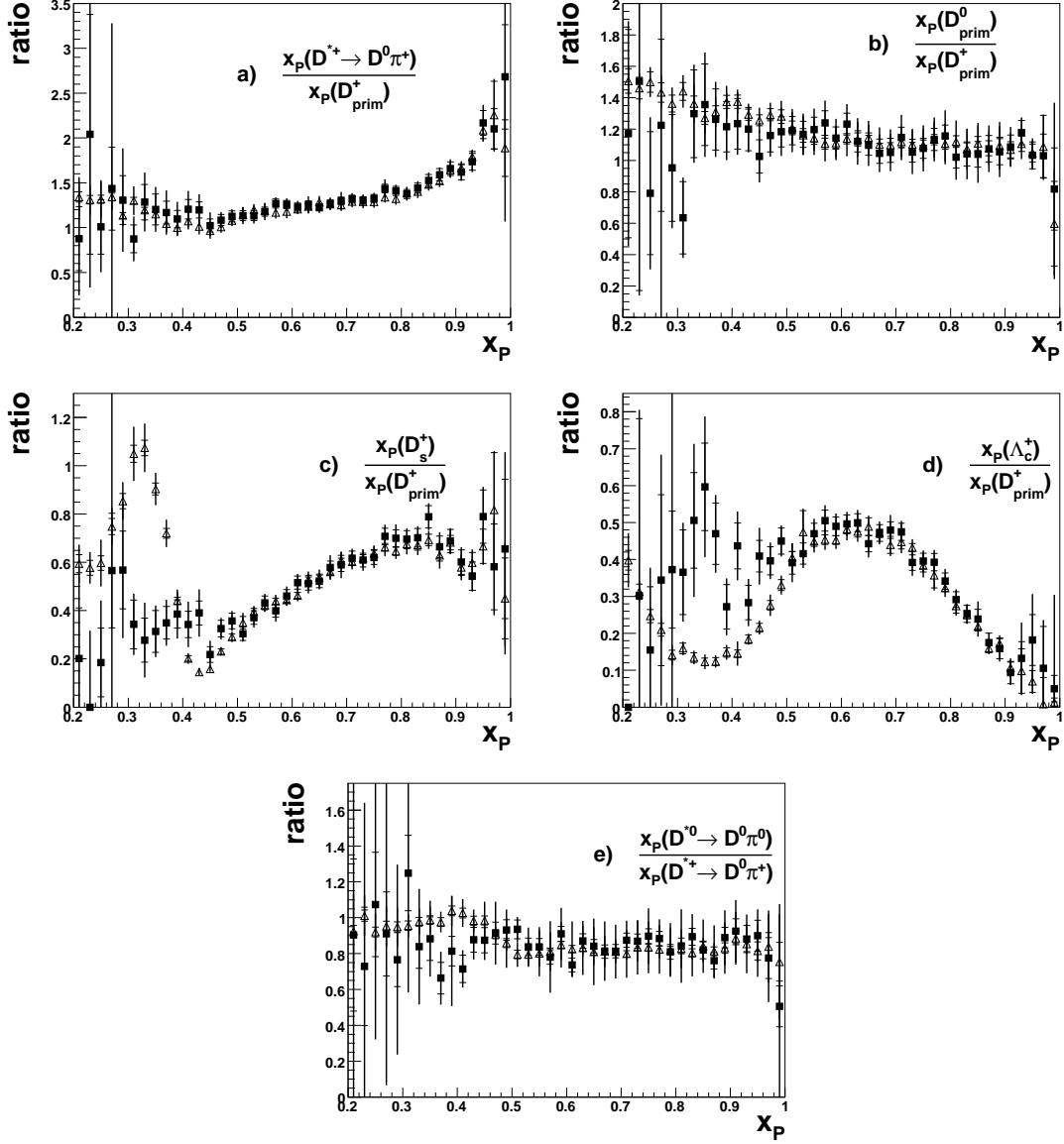| fragm. function	functional form	comment
Bowler	$N \frac{1}{z^{1+bm^2}}(1-z)^a \exp\left(-\frac{bm_\perp^2}{z}\right)$	a, b identical for all quarks
Lund	$N \frac{1}{z}(1-z)^a \exp\left(-\frac{bm_\perp^2}{z}\right)$	a, b identical for all quarks
Kartvelishvili	$N z^{\alpha_c}(1-z)$	
Collins-Spiller	$N \left(\frac{1-z}{z} + \frac{(2-z)\varepsilon_c'}{1-z}\right)(1+z^2)\left(1 - \frac{1}{z} - \frac{\varepsilon_c'}{1-z}\right)^{-2}$	
Peterson	$N \frac{1}{z}\left(1 - \frac{1}{z} - \frac{\varepsilon_c}{1-z}\right)^{-2}$	widely used

48

FIG. 10: The ratios $\mathrm{x_P}(D^{*+})/\mathrm{x_P}(D^+_{prim})$ and $\mathrm{x_P}(D^0_{prim})/\mathrm{x_P}(D^+_{prim})$ at the top, $\mathrm{x_P}(D^+_s)/\mathrm{x_P}(D^+_{prim})$ and $\mathrm{x_P}(\Lambda^+_c)/\mathrm{x_P}(D^+_{prim})$ in the middle and $\mathrm{x_P}(D^{*0})/\mathrm{x_P}(D^{*+})$ at the bottom. The open upward triangles represent on-resonance data, and the full squares with error bars represent continuum data. The inner (outer) error bars show the statistical (total) uncertainties.
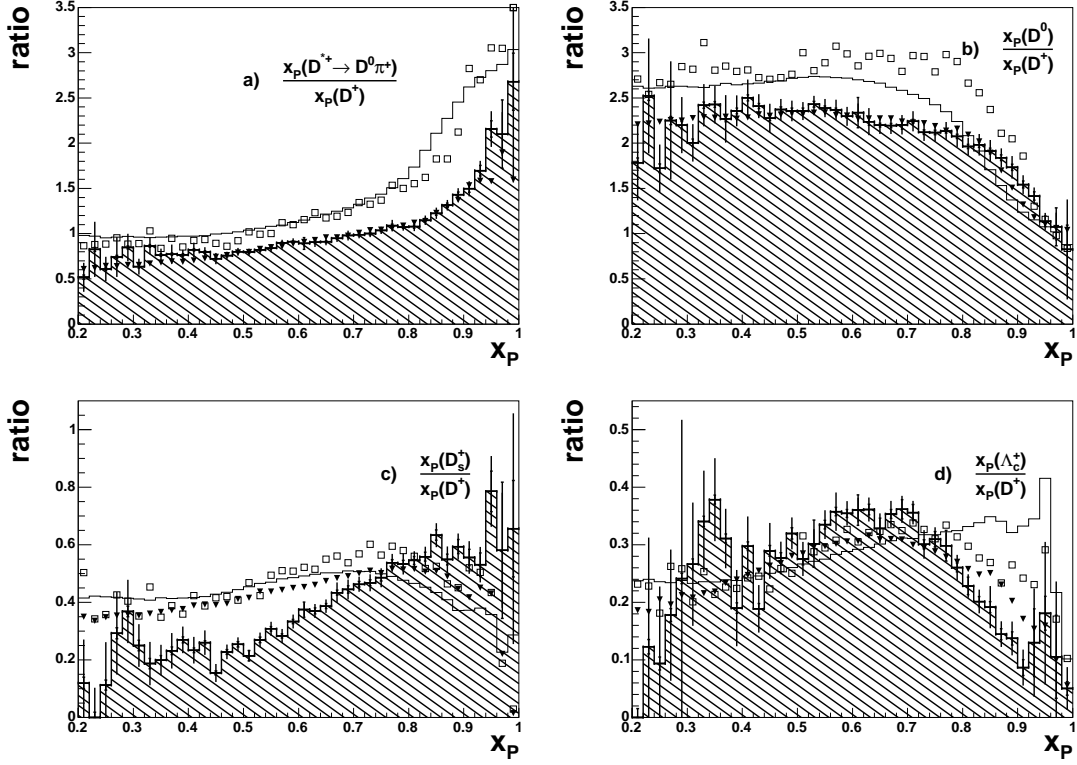
FIG. 11: The ratios $x_P(D^{*+})/x_P(D^+)$ in a), $x_P(D^0)/x_P(D^+)$ in b), $x_P(D_s^+)/x_P(D^+)$ in c) and $x_P(\Lambda_c^+)/x_P(D^+)$ in d). The hatched histograms represent the ratio for continuum data, the open histogram shows the distribution for the corresponding ratios from generic MC, the open squares show the predictions using the Bowler fragmentation function with default parameters. The full triangles show the predictions using the Bowler fragmentation function with a tuned value for the probability of producing a charmed meson with spin=1: **PARJ(13)** $= 0.59$.

TABLE XII: The minimum of the chi-squared distribution, χ^2_{min}, for MC samples reweighted to represent the fragmentation functions shown, varying their respective parameters. The number of degrees of freedom (d.o.f.) is also shown for each case.

	D^0	D^+	D_s^+	Λ_c^+	D^{*+}
	$\chi^2_{min}/d.o.f.$	$\chi^2_{min}/d.o.f.$	$\chi^2_{min}/d.o.f.$	$\chi^2_{min}/d.o.f.$	$\chi^2_{min}/d.o.f.$
Bowler	1327.0 / 59	188.4 / 60	730.7 / 55	269.1 / 60	541.8 / 55
Lund	1500.5 / 59	527.1 / 60	513.2 / 55	266.6 / 60	965.6 / 55
Collins and Spiller	3032.1 / 58	948.0 / 60	1412.5 / 55	2836.7 / 59	1540.7 / 54
Kartvelishvili	3210.4 / 59	861.4 / 60	735.3 / 55	390.7 / 60	1271.1 / 54
Peterson	5070.2 / 59	2229.6 / 60	829.6 / 55	1345.0 / 59	3003.0 / 54

TABLE XIII: The parameters of the fragmentation functions at the minimum of the $\chi^2/d.o.f.$ distributions .

		D^0	D^+	D_s^+	Λ_c^+	D^{*+}
	parameter	pars at min.	pars at min.	pars at min.	pars at min.	pars at min.
Bowler	$a\|b$	0.12 | 0.74	0.12 | 0.58	0.12 | 0.68	0.34 | 0.74	0.22 | 0.56
Lund	a	0.26	0.45	0.2	0.55	0.58
Collins and Spiller	ε'_c	0.04	0.055	0.04	0.04	0.075
Kartvelishvili	α_c	4.6	4	5.6	3.6	5.6
Peterson	ε_c	0.028	0.039	0.008	0.011	0.054

51